

Hunting for anti-solar differentially rotating stars using the Rossby number

An application to the *Kepler* field

Q. Noraz^{1*}, S. N. Breton¹, A. S. Brun¹, R. A. García¹, A. Strugarek¹, A. R. G. Santos^{2,3}, S. Mathur^{4,5} and L. Amard¹

¹ Département d'Astrophysique/AIM, CEA/IRFU, CNRS/INSU, Univ. Paris-Saclay & Univ. de Paris, 91191 Gif-sur-Yvette, France

² Instituto de Astrofísica e Ciências do Espaço, Universidade do Porto, CAUP, Rua das Estrelas, PT4150-762 Porto, Portugal

³ Department of Physics, University of Warwick, Coventry, CV4 7AL, UK

⁴ Instituto de Astrofísica de Canarias (IAC), E-38205 La Laguna, Tenerife, Spain

⁵ Universidad de La Laguna (ULL), Departamento de Astrofísica, E-38206 La Laguna, Tenerife, Spain

Received 28 April, 2022, Accepted 5 July, 2022

ABSTRACT

Context. Anti-solar differential rotation profiles have been found for decades in numerical simulations of convective envelopes of solar-type stars. These profiles are characterized by a slow equator and fast poles (i.e., reversed with respect to the Sun) and have been found in simulations for high Rossby numbers. Rotation profiles like this have been reported in evolved stars, but have never been unambiguously observed for cool solar-type stars on the main sequence. As solar-type stars age and spin down, their Rossby numbers increase, which could therefore induce a transition toward an anti-solar differential rotation regime before the end of the main sequence. Such a rotational transition will impact the large-scale dynamo process and the magnetic activity. In this context, detecting this regime in old main-sequence solar-type stars would improve our understanding of their magnetorotational evolution.

Aims. The goal of this study is to identify the most promising cool main-sequence stellar candidates for anti-solar differential rotation in the *Kepler* sample.

Methods. First, we introduce a new theoretical formula to estimate fluid Rossby numbers, Ro_f , of main-sequence solar-type stars. We derived it from observational quantities such as T_{eff} and P_{rot} , and took the influence of the internal structure into account. Then, we applied it on a subset of the most recent catalog of *Kepler* rotation periods, after removing subgiants and selecting targets with solar metallicity. Next, we considered the highest computed Ro_f and inspected each target individually to select the most reliable anti-solar candidate. Finally, we extended our study to stars with metallicities different from that of the Sun. To this end, we developed a formulation for Ro_f dependent on the metallicity index $[\text{Fe}/\text{H}]$ by using 1D stellar grids, and we also considered this compositional aspect for the selection of the targets.

Results. We obtain a list of the most promising stars that are likely to show anti-solar differential rotation. We identify two samples: one at solar metallicity, including 14 targets, and another for other metallicities, including 8 targets. We find that the targets with the highest Ro_f are likely to be early-G or late-F stars at about $\log_{10} g = 4.37$ dex.

Conclusions. We conclude that cool main-sequence stellar candidates for anti-solar differential rotation exist in the *Kepler* sample. The most promising candidate is KIC 10907436, and two other particularly interesting candidates are the solar analog KIC 7189915 and the seismic target KIC 12117868. Future characterization of these 22 stars is expected to help us understand how dynamics can impact magnetic and rotational evolution of old solar-type stars at high Rossby number.

Key words. Stars: rotation – Stars: fundamental parameters – Stars: evolution – Stars: solar-type – Sun: rotation – Sun: evolution – Techniques: photometric – Methods: observational – Methods: data analysis – Methods: analytical – Convection

1. Introduction

Observations of stellar rotation show that solar-type stars experience various phases of rotational evolution during their life (Gallet & Bouvier 2013). In particular, their angular momentum decreases during the main-sequence (MS) phase, likely due to mass loss associated with their magnetized stellar wind (see Schatzman 1962, Weber & Davis 1967, Mestel 1968 or Vidotto 2021 for a recent review). The resulting spin-down is observationally

well described by the Skumanich law $\Omega_* \propto t^{1/2}$ (Skumanich 1972) and enables estimating MS stellar ages from gyrochronology (Barnes 2003), within a given parameter space.

The evolution of the angular velocity Ω_* can strongly affect the internal dynamics of stars. In particular, numerical simulations show that the differential rotation (DR) profile changes as the star spins down (Brun et al. 2017, 2022). Fast-rotating models tend to exhibit Jupiter-like, cylindrical, or quenched rotation profiles, intermediately rotating models exhibit solar-type DR (fast equator, slow poles), and slow-rotating models switch to

* E-mail: quentin.noraz@cea.fr

an anti-solar DR regime, in which surface rotation exhibits fast poles along with a slow equator.

More generally, these DR transitions are well characterized by the dimensionless Rossby number Ro , which quantifies the amplitude of the advective transport over the Coriolis force. These different DR regimes are expected to significantly influence the internal dynamics of the star and its evolution. [Noraz et al. \(2022\)](#) and [Brun et al. \(2022\)](#) (hereafter [B22](#)) showed that simulations of solar-type dynamos change in nature depending on the rotational regime of their convective envelope. Low Ro models (fast rotators) tend to exhibit short (yearly) magnetic cycles, and intermediate Ro models tend to exhibit long (decadal) cycles. Finally, high Ro models (slow rotators) switching to an anti-solar DR regime are likely to exhibit stationary dynamos by losing their periodic magnetic reversals.

In addition, with the recent increase in the number of stars with measured rotation periods, it has been observed that MS stars undergo epochs of weakened (van Saders et al. 2016) or stalled braking (Curtis et al. 2020), deviating from the classical Skumanich law. Thus, techniques such as gyrochronology, which rely on the direct relation between rotation and age, need further investigations. For the apparently weakened braking at late ages, different physical explanations have been proposed. The first is a change in the dynamo process of slowly rotating stars, as suggested by recent observations (Metcalfé et al. 2019). It has been shown that the magnetic torque provided by stellar winds mostly depends on large-scale magnetic modes (Réville et al. 2015; Finley & Matt 2018). However, the observational characterization of stellar magnetic topologies is difficult (See et al. 2019), and recent studies of ab initio dynamo models do not report strong changes in large-scale magnetic topology that could support this scenario (Noraz et al. 2022, B22). A change in coronal properties could also explain this transition, making the wind less efficient to extract angular momentum (Ó Fionnagáin & Vidotto 2018). However, we still lack observational and theoretical constraints on the stellar mass-loss rate of MS stars, which would confirm or refute this option. In this context, it is crucial to understand what exactly occurs for the angular momentum loss of slowly rotating stars.

Finally, the possibility of observational bias has also been proposed because slower rotators might lose their surface spots. This would make the detection of stellar rotational modulations relatively difficult with photometric techniques. However, [Hall et al. \(2021\)](#) confirmed evidence of a weakened magnetic braking by using asteroseismology, which makes the possibility of a photometric-observational bias less probable. Still, observations of late weakened magnetic braking are currently under debate as other studies failed to find it for their respective samples (Lorenzo-Oliveira et al. 2019; do Nascimento Jr. et al. 2020). At the moment, rotation rates of old MS solar-type stars are therefore uncertain. This will influence the likelihood of finding anti-solar rotators.

The anti-solar DR regime has been observed in various numerical simulations of convective rotating spherical shells for several decades (Gilman 1977; Matt et al. 2011; Käpylä et al. 2011; Guerrero et al. 2013; Gastine et al. 2014; Fan & Fang 2014; Käpylä et al. 2014; Karak et al. 2015; Simitev et al. 2015; Mabuchi et al. 2015; Brun et al. 2017; Warnecke 2018; Strugarek et al. 2018; Viviani et al. 2019; Brun et al. 2022). Motivated by numerical results, different observational methods have been used so far to detect stellar DR: photometry, asteroseismology, and spectroscopy imaging. Using the latter, robust anti-solar detections have been obtained with Doppler imaging spectroscopy for red giants (see, e.g., Strassmeier et al. 2003, Kóvári et al.

2017 and references therein) and subgiant stars (Harutyunyan et al. 2016). However, no unambiguous detection of such a profile has been reported so far for solar-type stars on the MS. The starspot signature can be tracked in photometric light-curves in order to quantify the velocity gradient $\Delta\Omega$ along the latitudes. Using this approach, [Reinhold & Arlt \(2015\)](#) asserted their belief that anti-solar DR is possible in 13 *Kepler* targets. However, [Santos et al. \(2017\)](#) showed that this problem is likely degenerated in most cases, making a clear distinction of the DR regime uncertain without independent constraints. Using asteroseismic methods, [Benomar et al. \(2018\)](#) detected signatures that suggested anti-solar DR profiles in ten solar-type stars in the *Kepler* field, but the confidence level was not high enough to confirm detection. Thus, robust detections of anti-solar profiles are still pending for MS solar-type stars, and will need the scrutiny of the most promising targets with highly resolved data.

It is then instructive to assess whether the Sun or solar analogs could experience a change toward the anti-solar DR regime before they reach the end of their MS life. The solar fluid Rossby number Ro_f (see Sections 2.2 and 2.3) is currently thought to be between 0.6 and 0.9 according to recent numerical simulations in [B22](#), and the rotational transition is expected to be above $Ro_f = 1$. If the Sun were to strictly follow the Skumanich law (Skumanich 1972), its Ro_f would increase by a factor 1.48 by the end of the MS. It could then exceed unity enough for an anti-solar DR regime to be possible (Gastine et al. 2014; Brun et al. 2017). Old solar analogs could therefore exhibit anti-solar DR if this were detectable with current techniques. More generally, different effects can play a role for the Ro_f value that the star can reach for solar-type stars. On the one hand, the more massive a solar-type star, the more vigorous its convective motions. However, the highest-mass solar-type stars may never rotate slowly enough to enter the anti-solar DR regime during the MS (see Fig. 6 of [Amard et al. 2019](#)). On the other hand, the lower the mass of a solar-type star, the longer its MS lifetime and the higher its spin-down amplitude. Nevertheless, lower-mass stars tend to have lower Rossby numbers because their convective transport is weaker than their rotational constraint. Therefore, an intermediate-mass sweet spot is expected at which solar-type stars might be in the right parameter regime to counterbalance these two opposing effects and ultimately reach Ro_f , favoring the anti-solar DR regime.

The goal of the present work is to search for these stars. The *Kepler* mission ([Borucki et al. 2010](#)) has observed almost 200,000 targets during its four-year-long nominal mission. Tens of thousands of these stars exhibit photometric rotational modulation (e.g., [McQuillan et al. 2014](#); [Santos et al. 2019](#); [Santos et al. 2021](#)). Hence, the *Kepler* survey is currently the best-suited dataset in order to search for anti-solar rotating stars.

We identify the most promising targets for anti-solar DR detection in the sample of MS cool stars of the *Kepler* field. In Sect. 2 we present an improved theoretical derivation of the fluid Rossby number Ro_f compared to [Brun et al. \(2017\)](#), taking the internal structure of solar-type stars into account and extending the computation for the use of the effective temperature, T_{eff} . Then, we apply this formula to the *Kepler* catalog of [Santos et al. \(2019\)](#), (2021) (referred to as S19-21) in Sect. 3 for solar-metallic MS targets and select the highest Ro_f values. Next, we inspect each selected target individually and build a list of promising candidates, which are discussed. After this, we extend this method to other metallicities in Sect. 4. We finally discuss the limitations of our method in Sect. 5 and conclude in Sect. 6 by highlighting the most promising anti-solar candidates for a future characterization of these targets.

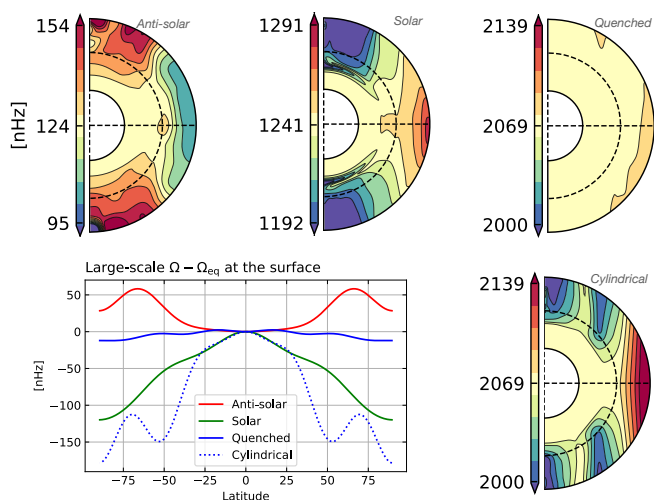


Fig. 1. Example of DR profiles that emerge in numerical simulations of stellar convective envelopes. The top panels show DR profiles achieved in MHD models of B22, from high to low Rossby numbers (left to right). The bottom right profile is characteristic of low Rossby numbers in hydrodynamics models of Brun et al. (2017). The symmetric part of the surface velocity from these meridional cuts is illustrated in the bottom left panel for all profiles.

2. Differential rotation states and Rossby number

2.1. Differential rotation profiles from numerical simulations

Numerical simulations of stellar convective envelopes yield various DR profiles, depending on the Rossby number (see Brun & Browning 2017 for a review). The dimensionless Rossby number Ro parameterizes the influence of the rotation on the dynamics of a system. In a star, it quantifies the impact of the Coriolis force on turbulent convective motions. Convective motions can collectively transport angular momentum (through Reynolds stresses) to establish a large-scale DR. The characteristics of their DR therefore depend on Ro , as illustrated in Fig. 1. For low Rossby numbers (right panels), profiles are highly constrained by the influence of the rotation. In the bottom right panel, a hydrodynamical case shows a cylindrical profile, with alternating prograde and retrograde zonal jets (also called Jupiter-like jets). This alignment along the vertical axis results from the Taylor-Proudman constraint that was achieved in fast-rotating convective envelopes (Gilman 1975; Elliott et al. 2000; Miesch et al. 2006). The DR amplitude can be quenched when a magnetic field is considered to be in such a regime (Ω -quenching) because of the Lorentz force feedback (Brun 2004, B22). Around intermediate Sun-like Rossby numbers, typical solar and conical DR profiles are found, with fast equator and slow poles (top middle panel). Finally, anti-solar profiles with a slow equator and fast poles are found for high Rossby numbers (top left panel). The rotational transition from solar-type and anti-solar profiles lies around $Ro_f = 1$ (Gastine et al. 2014). We show in the bottom left panel the symmetric part of the surface DR that was achieved in these simulations. The amplitude of the shear of the anti-solar regime (about 50 nHz, i.e., 0.03 rad/days) is similar to that of the solar regime, which means that it might be detected with current capabilities (e.g., Reinhold & Gizon 2015).

2.2. Rossby number definitions

Different definitions of the Rossby number exist and are used in the community. While their absolute values can differ, they gen-

erally scale with each other (Landin et al. 2010, B22).

First, the stellar Rossby $Ro_s = \frac{P_{\text{rot}}}{\tau_{\text{conv}}}$ is often used in the observational context. It compares two characteristic timescales, the rotation period of the star $P_{\text{rot}} = 2\pi/\Omega_*$ and its convective overturning time τ_{conv} . Rotation can be measured directly (see, e.g., Sect. 4.1 of Brun & Browning 2017 and Sect. 7 of García & Ballot 2019 for reviews), but τ_{conv} has to be inferred from stellar models, considering mass, spectra, and chemical composition (see, e.g., Noyes et al. 1984, Fig. 6 of Cranmer & Saar 2011, or Corsaro et al. 2021). Furthermore, τ_{conv} can be computed at different depths in the star, which could also explain some differences in the absolute Rossby values.

An alternative is the fluid Rossby $Ro_f = \omega/2\Omega_* = \omega P_{\text{rot}}/4\pi$, which we chose to consider in this study, and where ω is the vorticity. It is often used to characterize numerical simulations because it quantifies a force balance between nonlinear advection and Coriolis acceleration in the Navier-Stokes equation. Once again, the vorticity ω is not observed and has to be deduced from models. Similarly to Ro_s , this quantity depends on the stellar depth that is chosen. We therefore propose in the next subsection to infer it from observable quantities, and to normalize it to the solar value in order to alleviate a dependence on the Ro definition we chose.

2.3. Fluid Rossby number based on observable quantities

First, we derived an analytical formulation of Ro_f as a function of the stellar mass M_* and the rotation rate Ω_* , following Brun et al. (2017). We then extended it by considering the effective temperature T_{eff} in order to infer Ro_f from observations. Next, we calibrated it with scaling laws from stellar evolution models and compared the resulting trend with 3D global numerical simulations of stellar convection. Finally, we took a structural aspect into account in order to extend the mass range on which we can apply the final formula. This is presented in Eq. 18.

2.3.1. Fluid Rossby number as a function of M_* and P_{rot}

Based on fluid dynamics, Ro_f can be estimated as

$$Ro_f = \omega/2\Omega_* \simeq \frac{v_{\text{conv}}}{2\Omega_* D}, \quad (1)$$

where v_{conv} is the representative convective velocity participating in the Reynolds stresses, D is a characteristic length scale, and Ω_* the rotation rate of the star. In general, D is considered to be the stellar radius R_* or the convection zone (CZ) thickness. Following the mixing-length theory (MLT) argument in Brun et al. (2017), the enthalpy flux F_{en} transported by convective cells is the main source of energy transport through the CZ of cool stars. We can relate F_{en} to the velocity by assuming that $F_{\text{en}} \sim \rho v^3$, by analogy to the kinetic energy flux. Hence, we have $L_* \propto \rho_{\text{BCZ}} v_{\text{conv}}^3 R_*^2$, with ρ_{BCZ} the density at the base of the convection zone (BCZ). The fluid Rossby number is then proportional to

$$Ro_f \propto \left(\frac{L_*}{\rho_{\text{BCZ}} R_*^5} \right)^{1/3} \Omega_*^{-1}. \quad (2)$$

We used the well-known homology relations on the MS (Kippenhahn et al. 2012), such as

$$L_* \propto M_*^m \quad \text{and} \quad R_* \propto M_*^n, \quad (3)$$

and we parameterized ρ_{BCZ} during the MS, as $\rho_{BCZ} \propto M_*^p$, to obtain

$$Ro_f \propto M_*^{(m-5n-p)/3} \Omega_*^{-1}, \quad (4)$$

with $m, n > 0$ and $p < 0$, but undetermined for now. We obtained an expression of Ro_f based on the mass and rotation rate of a solar-type star. We now proceed and derive its equivalent formulation based on observable quantities.

2.3.2. Observable quantities

One main point of this paper is to infer the fluid Rossby number through the use of T_{eff} rather than M_* . The determination of M_* is model dependent and therefore has larger uncertainties (Lebreton & Goupil 2014). On the other hand, T_{eff} can be directly measured with high precision through spectroscopy (see, e.g., APOGEE DR17; Abdurro'uf et al. 2022).

Hence, we now consider the link between stellar luminosity L_* and global quantities, such as the stellar radius R_* and T_{eff} ,

$$L_* = 4\pi R_*^2 \sigma T_{\text{eff}}^4, \quad (5)$$

where σ is the Stefan–Boltzmann constant. Using again the homology relations in Eq. 3, we then obtain the relation

$$T_{\text{eff}} \propto M_*^{(m-2n)/4}, \quad (6)$$

which subsequently gives

$$Ro_f \propto T_{\text{eff}}^{\frac{4}{m-2n} \left(\frac{m-5n-p}{3} \right)} \Omega_*^{-1}. \quad (7)$$

We now have two analytical expressions of the Ro_f of a solar-type star, based on Ω_* , along with M_* or T_{eff} (Eqs. 4 and 7, respectively). We now compute the corresponding exponents based on various numerical models.

2.3.3. Inferring scaling indexes from numerical models

In order to compute exponents of Eqs. 4 and 7, we performed linear regression fits on the evolutionary tracks from Amard et al. (2019) (hereafter A19). We focused on solar-type stars and therefore considered masses ranging from 0.4 to $1.3M_\odot$ and a metallicity index [Fe/H] from -1 to $+0.3$ dex. This yields $m = 4.66 \pm 0.06$, $n = 1.16 \pm 0.01$, and $p = -9.28 \pm 0.37$ for the MS. When applied to Eqs. 4 and 7, we obtain

$$Ro_f \propto M_*^{2.71 \pm 0.13} \Omega_*^{-1} \propto T_{\text{eff}}^{4.64 \pm 0.23} \Omega_*^{-1}. \quad (8)$$

For the sake of robustness, we now performed a multiparameter linear regression fits directly on the fluid Rossby numbers achieved by convective motions in the published 3D magneto-hydrodynamic (MHD) global simulations of B22. We directly computed $Ro_f = \omega/2\Omega_*$ from them, and assessed how it scales with Ω_* , M_* , and T_{eff} (see the tabulated Ro_f values in B22). B22 modeled solar-type stars for a mass range of $0.5 < M_* < 1.1M_\odot$, a temperature range of $4030 \text{ K} < T_{\text{eff}} < 6030 \text{ K}$ at different rotation rates Ω_* , and for the solar composition. This gives

$$Ro_f \propto \frac{M_*^{1.63 \pm 0.24}}{\Omega_*^{0.9 \pm 0.06}} \propto \frac{T_{\text{eff}}^{3.2 \pm 0.4}}{\Omega_*^{0.9 \pm 0.05}}. \quad (9)$$

We note that the exponents from Eq. 8 computed from a broad sample of solar-type 1D models do not match with what is inferred from ab initio convective simulations in Eq. 9. The stellar structure of solar-type stars can significantly change within a

wide range of masses and metallicities, which subsequently impacts the Ro_f value. In particular, we note that 1.2 and $1.3M_\odot$ 1D models notably impact exponents inferred from linear fits. In the next section, we therefore add the structural aspect of solar-type stars in the analytical development of Ro_f . The specific effect of metallicity is addressed in Section 4.

2.3.4. Structural fluid Rossby number

In an attempt to take the stellar structure into account, the characteristic length D (Eq. 1) can be taken as the middle of the convective envelope $R_{\text{mid}} = 0.5(R_{BCZ} + R_*) = 0.5R_*(\alpha + 1)$, where $\alpha = R_{BCZ}/R_*$ is the aspect ratio of the radiative interior of the cool star. Following the derivation of the previous section, we find

$$L_* \propto \bar{\rho} v_{\text{conv}}^3 R_{\text{mid}}^2 \propto \bar{\rho} v_{\text{conv}}^3 (1 + \alpha)^2 R_*^2, \quad (10)$$

with $\bar{\rho}$ the averaged density in the convective envelope. The combination of Eqs. 1 and 10 gives

$$Ro_f \propto (1 + \alpha)^{-5/3} \left(\frac{L_*}{\bar{\rho} R_*^5} \right)^{1/3} \Omega_*^{-1}. \quad (11)$$

We now express the average density of the CZ as its mass divided by its volume,

$$\bar{\rho} \sim \frac{M_{CZ}}{V_{CZ}} \propto \frac{(1 - \beta)M_*}{(1 - \alpha^3)R_*^3}, \quad (12)$$

where $\beta = M_{BCZ}/M_*$ is the relative mass of the radiative interior. Injecting it into Eq. 11 leads to

$$Ro_f \propto S(\alpha, \beta) \left(\frac{L_*}{M_* R_*^2} \right)^{1/3} \Omega_*^{-1}, \quad (13)$$

$$\text{where } S(\alpha, \beta) = \left(\frac{1 - \alpha^3}{(1 - \beta)(1 + \alpha)^5} \right)^{1/3} \quad (14)$$

is a structure term depending on the structure parameters α and β . We finally assume that the stellar structure does not change during the MS, which only leaves a dependence on the stellar mass at first approximation. We can then parameterize it as $S(\alpha, \beta) \propto M_*^q$ during the MS, which yields

$$Ro_f \propto M_*^a \Omega_*^{-1} \text{ where } a = \frac{m - (2n + 1)}{3} + q, \quad (15)$$

with $q > 0$ a priori, but undetermined for now. Using previous development, this gives

$$Ro_f \propto T_{\text{eff}}^b \Omega_*^{-1} \text{ where } b = \frac{4}{m - 2n} \left(\frac{m - (2n + 1)}{3} + q \right). \quad (16)$$

Similarly to Sect. 2.3.3, we computed the exponents of Eqs. 15 and 16 from the evolutionary tracks of A19, considering $0.4 \leq M_* \leq 1.3M_\odot$. Linear regression fits yield $m = 4.66 \pm 0.03$, $n = 1.16 \pm 0.01$ and $q = 1.48 \pm 0.05$ for the MS (see the fits and values in Fig. C.1). Hence, applying these exponents to Eqs. 15 and 16, we finally obtained the following relations:

$$Ro_f \propto \frac{M_*^{1.93 \pm 0.05}}{\Omega_*} \propto \frac{T_{\text{eff}}^{3.29 \pm 0.09}}{\Omega_*}. \quad (17)$$

We note that it is now closer to what we derived from numerical simulations in Eq. 9, especially with T_{eff} .

Considering $T_{\text{eff},\odot} = 5772$ K (Prša et al. 2016), $P_{\text{rot},\odot} = 27.3$ days, a convenient formula we used is

$$\frac{Ro_f}{Ro_{f,\odot}} = \left(\frac{P_{\text{rot},*}}{P_{\text{rot},\odot}} \right) \times \left(\frac{T_{\text{eff}}}{T_{\text{eff},\odot}} \right)^{3.29}. \quad (18)$$

Using the solar values as reference prevents introducing a bias related to the dependence on the convention chosen for the Ro definition (see Sect. 2.2). The scaling law in Eq. 18 can then readily be applied to estimate the Ro_f of a star with respect to the Sun. We now estimate Ro_f of those *Kepler*-field stars for which a rotation period has been measured.

3. Application to *Kepler* stars with solar metallicity

In this section, we consider solar metallicity targets. Targets with other metallicities are addressed in Sect. 4.

3.1. The *Kepler* rotation catalog

The stellar surface rotation catalog compiled by S19-21 provides rotation periods and photometric magnetic activity proxies (García et al. 2010; Mathur et al. 2014) for 55,232 FGKM MS and subgiant *Kepler* targets. It extends the catalog from McQuillan et al. (2014) with 24,182 new detections and populates the slow-rotator region for all spectral types. This is particularly important for this work. The S19-21 catalog was built by implementing the method described in Ceillier et al. (2016, 2017), which combines the outputs of the autocorrelation function and of a time-frequency analysis. Machine-learning methods and visual inspections have been performed in order to ensure the reliability of the results (Breton et al. 2021).

The S19-21 catalog includes three subsamples. The first subsample (aliased I) corresponds to targets that are classified as solar-type stars in the Mathur et al. (2017) and Berger et al. (2020) (hereafter B20) stellar property catalogs. Stars for which their properties disagree are gathered in the two last subsamples (aliased II and III). We decided here to consider only subsample I, which represents 50,656 targets. We also considered M_* and T_{eff} proposed in S19-21, which originated from B20.

3.2. Data processing

First, in order to only select solar-metallicity stars, we extracted the metallicity index [Fe/H] for each star in the rotation catalog S19-21. For the sake of accuracy, we took [Fe/H] from the APOGEE database (DR16: Ahumada et al. 2020, DR17: Abdurro'uf et al. 2022), LAMOST (Zhao et al. 2012; Cat et al. 2015; Zong et al. 2018), or B20 in this order of priority for each target. We refer to Sect. 3.1 from Mathur et al. (2022) for more details. In this section, we consider stars at solar metallicity as stars with $-0.1 \text{ dex} < [\text{Fe}/\text{H}] < 0.1 \text{ dex}$. This means 16,258 stars of the 50,656 targets that were considered.

The criterion developed in Eq. 18 applies only to MS stars. When it is blindly applied to pre-main-sequence (PMS) stars in the stellar evolution grid of A19, we find a maximum $Ro_f/Ro_{f,\odot}$ of 0.291, which is well below the anti-solar DR threshold above 1. Therefore, no explicit filtering of PMS stars is necessary because these stars are not expected to harbor anti-solar DR due to their fast rotation (Emeriau-Viard & Brun 2017). Because the relations are derived for MS stars and because of the way in which stars evolve past the terminal age main sequence (TAMS), we also excluded subgiants from our sample. Following S19-21, we took the transition between MS and the subgiant branch

from evolutionary tracks obtained from A19 (see Appendix A for more details). Moreover, no subgiants for $M < 0.8M_{\odot}$ up to 13.7 Gyr are detected in these tracks. Hence, we assumed here that subgiants do not already exist at $\log_{10}g > 4.4$.

We also excluded stars that are flagged as type 1 classical pulsators/close binary (CP/CB) candidates in the S19-21 catalog. The characteristic period extracted from the light curves of these stars is likely to be distinct from the rotational behavior of single stars.

Finally, we only considered targets for which $0.4 \leq M_* \leq 1.3 M_{\odot}$ because this is the validity range for Eq. 18. The various data-processing steps presented in this section yielded a set of 12,517 stars. We then computed Ro_f for all stars in this sample.

3.3. Most promising targets at solar metallicity

Using Eq. 18, we selected all targets with $Ro_f/Ro_{f,\odot}$ above a given threshold. The anti-solar DR is expected to appear in a regime in which the dominant convective motions that transport angular momentum within the CZ are weakly influenced by the global rotation of the star (see Sect. 2.1). To do this, we placed a threshold at $Ro_f \geq 1.3$ to ensure that we were in this regime. For instance, $Ro_f = 1.24$ is the lowest Ro_f found in B22 models experiencing an anti-solar regime. Then, we considered two possible values $Ro_{f,\odot} = \{0.6; 0.9\}$ according to the current uncertainties on solar convection, known as the convective conundrum (Hanasoge et al. 2015). The lower value 0.6 corresponds to the value needed to obtain a decadal solar-type magnetic cycle in the MHD numerical simulations of B22, and 0.9 is the value that is effectively obtained in the solar regime in this same set of simulations. This gave us two thresholds $Ro_f/Ro_{f,\odot} = \{2.167; 1.444\}$, which define two samples that we refer to as the conservative and optimistic sample respectively. To ensure the reliability of this method, we computed the uncertainties and took them into account. Hence, a target was selected only if its normalized Rossby value from Eq. 18 had a lower limit above the given threshold.

This selection gave us 62 targets in the optimistic sample, 12 of which belonged to the conservative sample. We individually inspected them using the following method. We first considered the field of view (FoV) in the *Kepler* Asteroseismic Science Operations Center (KASOC) database¹ (Kjeldsen et al. 2010).

1. If the considered target was within the halo of a brighter star, we did not consider it because the T_{eff} or P_{rot} measurements might be biased.
2. We then ensured that no neighboring stars lay in a FoV of $40''$ centered on the target. The image scale of *Kepler* is 3.98 arcseconds per pixel, and the total acquisition FoV is a square of 10 pixels at a side (Van Cleve & Caldwell 2016). If neighbors with a similar magnitude were found, we considered the photometric aperture to ensure that the light curve of the considered target was not polluted. If this was not the case, we did not consider it.
3. Next, we studied the shape of the target in the FoV to avoid considering close binary systems.
4. Finally, we visually inspected the light curve and respective rotation diagnostics as indicated in Appendix B in order to ensure the reliability of the detected P_{rot} value.

The different results of these inspections are summarized for each target at solar metallicity in Appendix B.

After ensuring the reliability of the computed fluid Rossby value with previous inspections, we found 14 stellar candidates

¹ The KASOC database can be accessed at <http://kasoc.phys.au.dk>

Table 1. List and stellar parameters of anti-solar candidates at the solar metallicity

KIC	$\log_{10}g$	T_{eff} [K]	P_{rot} [days]	$Ro_f/Ro_{f,\odot}$	[Fe/H]	M_* [M_{\odot}]	S_{ph} [ppm]	Zfl	Sfl
10907436	$4.25^{+0.04}_{-0.03}$	$6364.3^{+137.1}_{-141.9}$	48.4 ± 3.9	$2.44^{+0.26}_{-0.26}$	$-0.07^{+0.03}_{-0.03}$	$1.22^{+0.06}_{-0.06}$	86.5 ± 3.2	1	2
8194513	$4.40^{+0.03}_{-0.04}$	$6030.1^{+121.2}_{-119.4}$	44.5 ± 3.6	$1.88^{+0.20}_{-0.20}$	$-0.05^{+0.13}_{-0.16}$	$1.06^{+0.06}_{-0.07}$	751.6 ± 17.9	2	1
6068129 ⁺	$4.40^{+0.04}_{-0.04}$	$5838.9^{+110.8}_{-110.8}$	49.4 ± 8.6	$1.88^{+0.35}_{-0.35}$	$-0.01^{+0.14}_{-0.16}$	$1.01^{+0.07}_{-0.08}$	588.6 ± 14.1	2	1
12117868 [*]	$4.24^{+0.04}_{-0.04}$	$6068.0^{+113.4}_{-114.8}$	42.5 ± 5.0	$1.84^{+0.24}_{-0.24}$	$-0.04^{+0.01}_{-0.01}$	$1.09^{+0.07}_{-0.07}$	71.7 ± 1.9	0	1
11912541	$4.08^{+0.04}_{-0.05}$	$5884.5^{+113.9}_{-117.9}$	46.4 ± 3.9	$1.81^{+0.19}_{-0.19}$	$0.03^{+0.14}_{-0.16}$	$1.13^{+0.11}_{-0.09}$	419.0 ± 10.9	2	1
3746157	$4.31^{+0.04}_{-0.04}$	$5863.5^{+115.2}_{-110.8}$	46.1 ± 5.3	$1.78^{+0.23}_{-0.23}$	$0.01^{+0.01}_{-0.01}$	$1.03^{+0.07}_{-0.07}$	446.7 ± 9.8	1	1
8245631	$4.14^{+0.05}_{-0.05}$	$5783.2^{+124.0}_{-123.4}$	48.0 ± 7.7	$1.77^{+0.31}_{-0.31}$	$0.03^{+0.17}_{-0.16}$	$1.05^{+0.10}_{-0.08}$	380.2 ± 11.5	2	1
10670661	$4.33^{+0.04}_{-0.04}$	$5832.4^{+111.8}_{-108.6}$	46.4 ± 7.5	$1.76^{+0.30}_{-0.30}$	$0.00^{+0.16}_{-0.15}$	$1.01^{+0.08}_{-0.08}$	277.2 ± 8.1	2	1
6850029 ⁺	$4.44^{+0.04}_{-0.04}$	$5640.5^{+102.5}_{-99.8}$	51.1 ± 4.9	$1.73^{+0.20}_{-0.19}$	$-0.01^{+0.14}_{-0.16}$	$0.94^{+0.06}_{-0.07}$	473.5 ± 12.1	2	1
11028172	$4.21^{+0.04}_{-0.04}$	$5654.9^{+110.7}_{-106.1}$	49.8 ± 5.7	$1.70^{+0.22}_{-0.22}$	$0.03^{+0.16}_{-0.17}$	$0.97^{+0.07}_{-0.07}$	387.9 ± 10.2	2	1
4265609	$4.34^{+0.04}_{-0.04}$	$5932.0^{+113.8}_{-111.4}$	42.1 ± 1.4	$1.69^{+0.12}_{-0.12}$	$-0.05^{+0.03}_{-0.03}$	$1.03^{+0.07}_{-0.07}$	466.8 ± 11.4	1	1
7908114	$4.25^{+0.05}_{-0.06}$	$5767.1^{+124.3}_{-118.8}$	46.1 ± 4.7	$1.68^{+0.21}_{-0.21}$	$0.03^{+0.14}_{-0.17}$	$1.00^{+0.08}_{-0.08}$	284.5 ± 10.9	2	1
7428723 ⁺	$4.40^{+0.04}_{-0.05}$	$5826.8^{+107.0}_{-105.5}$	44.2 ± 5.3	$1.67^{+0.22}_{-0.22}$	$-0.01^{+0.14}_{-0.16}$	$1.00^{+0.07}_{-0.07}$	606.2 ± 15.6	2	1
(7189915) ⁺	$4.43^{+0.04}_{-0.05}$	$5739.0^{+104.8}_{-101.5}$	(44.5 ± 5.0)	($1.60^{+0.20}_{-0.20}$)	$-0.02^{+0.14}_{-0.15}$	$0.97^{+0.06}_{-0.07}$	453.4 ± 14.0	2	1

Notes. We recapitulate here the main parameters for the anti-solar candidates at solar metallicity. From the left, we show the *Kepler* Input Catalog (KIC) identification, the surface gravity logarithm $\log_{10}g$, the effective temperature T_{eff} , the rotation period P_{rot} , the normalized fluid Rossby number value from Eq. 18, the metallicity index [Fe/H], the mass M_* , and the photometric magnetic activity proxy S_{ph} . The metallic flag Zfl indicates the origin of the quoted [Fe/H] value (APOGEE (0), LAMOST (1), or B20 (2)). The last flag Sfl is a sample flag indicating whether the target is in the optimistic (1) or conservative (2) sample. Values within parentheses are further discussed in the text, and the exponent on the KIC indicates either a solar analog (+) or a seismic target (*).

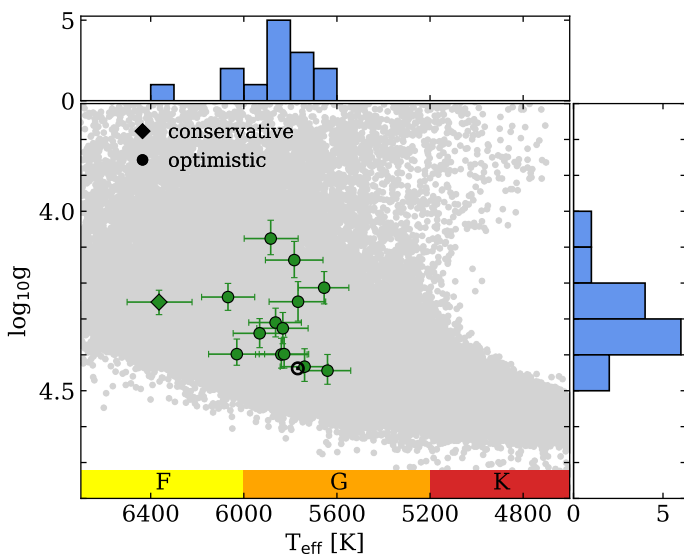


Fig. 2. Kiel diagram (T_{eff} vs. $\log_{10}g$) for anti-solar DR candidates at solar metallicity. The conservative and optimistic samples are illustrated with green diamonds and circles, respectively. The circled dot represents the Sun, and spectral types are indicated on the T_{eff} -axis. Spectral types are defined here with the standard Harvard Spectral Classification (see, e.g., [Habets & Heintze 1981](#) for more details). Histograms on the x- and y-axes correspond to the T_{eff} and $\log_{10}g$ distributions for the candidates shown in green. We illustrate all rotators from the S19-21 catalog with gray dots for comparison.

at solar metallicity that were likely to be in an anti-solar DR regime. We illustrate them in a Kiel diagram in Fig. 2. Only one of the 14 candidates that are in the optimistic sample is in the conservative sample (diamond marker). We plot the distributions including the 14 targets on both axes, which show that high Ro_f

targets are likely to be found around the medians $\log_{10}g = 4.32$ and $T_{\text{eff}} = 5836$ K (early-G spectral type) for old MS cool stars with solar metallicity. We summarize the stellar parameters of each target in Table 1.

We first note that all anti-solar candidates have rotational periods P_{rot} between 42.1 and 51.1 days, effective temperatures T_{eff} from 5640 to 6365 K (early-G and late F-type stars), and masses M_* ranging from 0.94 to 1.22 M_{\odot} . Because all stellar gravities, $\log_{10}g$, lie between 4.08 and 4.44 dex, these targets seem consistent with old MS stars. We then note that KIC 6068129, 6850029, and 7428723 can be considered as solar analogs according to their stellar parameters. We considered stars as solar analogs when their parameters (including uncertainties) fit within ranges of 250 K around $T_{\text{eff},\odot} = 5772$ K and 0.10 dex around $\log_{10}g_{\odot} = 4.44$. Slightly less conservative definitions can be adopted. We refer to [Cayrel de Strobel \(1996\)](#) for an extensive discussion. Another noteworthy target is KIC 12117868, which is a seismic target ([García et al. 2014](#)). Next, we verified the value of the S_{ph} index, which is a proxy of photometric magnetic activity computed as defined in [Mathur et al. \(2014\)](#). S_{ph} of these stars reaches a maximum of 751.6 ppm and mostly lies in the solar range $S_{\text{ph},\odot} = 50$ –600 ppm ([Salabert et al. 2017](#)). The maximum $Ro_f/Ro_{f,\odot}$ value for these stars is 2.44 and is reached by KIC 10907436, which thus seems to be the most promising candidate for showing anti-solar DR in the sample of stars at solar metallicity.

In Table 1 we consider KIC 7189915, which should have been excluded from the optimistic sample. This target was first selected thanks to its high Ro_f value, which is partly due to a relatively long $P_{\text{rot}} = 51.1 \pm 4.7$ days given by S19-21. During individual inspections of it, we revised this value and now consider $P_{\text{rot}} = 45 \pm 5$ days, which yields $Ro_f/Ro_{f,\odot} = 1.60^{+0.20}_{-0.20}$ when Eq. 18 is recomputed with the new period. Consequently, the new $Ro_f/Ro_{f,\odot}$ lower limit (1.40) is slightly below the thresh-

old $1.3/0.9 = 1.44$, and we should accordingly strictly not consider this target in Table 1. However, we chose to include it because of its relatively high $Ro_f/Ro_{f,\odot}$ value and because we are confident through visual inspection of the target that this new period value is reliable. This makes it a promising candidate. Most importantly, however, its parameters are very close to the solar parameters, which makes it an interesting target to investigate because it is probably older than the Sun according to the gyrochronology. As a first guess of its age, we used luminosity, effective temperature, metallicity, and rotation period to interpolate in the grid of Amard et al. (2019) and found an estimate of about 9.5 ± 0.5 Gyr.

4. Extended sample at different metallicities

After applying our data-processing steps and Ro_f selection to 16,258 solar metallicity targets, we extended our interest to stars with other metallicities and considered all 50,656 rotators in subsample I of S19-21. This implies that the variations in Ro_f as a function of metallicity were taken into account. We expressed this dependence as a function of the metallicity index $[Fe/H]$ in order to keep the Ro_f formula in terms of observable quantities.

4.1. Fluid Rossby number including metallicity

In this subsection, we add the metallicity index $[Fe/H]$ to the analytical development of the structural fluid Rossby number. Because homology relations (Eq. 3) should also depend on the composition (Kippenhahn et al. 2012), we adapted them by explicitly adding $[Fe/H]$, such that

$$L_* \propto M_*^{m_1} ([Fe/H] + 2)^{m_2} \quad \text{and} \quad R_* \propto M_*^{n_1} ([Fe/H] + 2)^{n_2}, \quad (19)$$

with m_2 and n_2 undetermined for now. Moreover, the metallicity impacts the structure of the star. A higher abundance of heavy elements increases the opacity in the star, making radiative transfer less effective. This results in an increase in the temperature gradient (Maeder 2009). This leads to a deeper convective envelope and a cooler star (Karoff et al. 2018; Amard et al. 2019) and slower convective speeds at the BCZ, which subsequently impacts the Rossby number (Amard & Matt 2020; See et al. 2021). We therefore took the dependence on $[Fe/H]$ in the structural aspect into account as well by parameterizing $S(\alpha, \beta)$ such that

$$S(\alpha, \beta) \propto M_*^{q_1} ([Fe/H] + 2)^{q_2}. \quad (20)$$

Similarly, we obtained

$$Ro_f \propto M_*^{a_1} ([Fe/H] + 2)^{a_2} \Omega^{-1}$$

$$\text{with} \quad \left\{ \begin{array}{l} a_1 = q_1 + \frac{m_1 - (2n_1 + 1)}{3} \\ a_2 = q_2 + \frac{m_2 - 2n_2}{3} \end{array} \right\}. \quad (21)$$

Substituting Eqs. 19 into Eqs. ?? and 21 gives

$$M_* \propto T_{\text{eff}}^{4/(m_1 - 2n_1)} ([Fe/H] + 2)^{(2n_2 - m_2)/(m_1 - 2n_1)}, \quad (22)$$

$$Ro_f \propto T_{\text{eff}}^{b_1} ([Fe/H] + 2)^{b_2} \Omega^{-1}$$

$$\text{with} \quad \left\{ \begin{array}{l} b_1 = \frac{4a_1}{m_1 - 2n_1} \\ b_2 = a_1 \frac{2n_2 - m_2}{m_1 - 2n_1} + a_2 \end{array} \right\}. \quad (23)$$

Multiparameter regression fits on the evolutionary tracks of A19 (see fits and values in Fig. C.1) gave m_1 , n_1 , and p_1 equivalent to what was found in Sect. 3. In addition, we find $m_2 = -1.00 \pm 0.04$, $n_2 = 0.01 \pm 0.01$, and $q_2 = -0.81 \pm 0.08$. It therefore appears that the stellar luminosity L_* is inversely proportional to the metallicity index $[Fe/H]$. This is due to the increase in opacity with higher $[Fe/H]$ because of the presence of elements with several atomic levels or ionization states. It also appears that the stellar radius R_* is nearly independent of the metallicity, regardless of the mass M_* considered (see Fig. C.1). We further note that the structure factor S decreases with $[Fe/H]$, which means that the CZ thickness increases with metallicity. Introducing these values in Eqs. 21 and 23 leads to

$$Ro_f \propto \frac{M_*^{1.93 \pm 0.05} ([Fe/H] + 2)^{-1.15 \pm 0.08}}{\Omega_*} \quad \text{and}$$

$$Ro_f \propto \frac{T_{\text{eff}}^{3.29 \pm 0.09} ([Fe/H] + 2)^{-0.31 \pm 0.09}}{\Omega_*}. \quad (24)$$

We find that the Ro_f value is inversely proportional to the metallicity index $[Fe/H]$, which is consistent with what has been observed by See et al. (2021).

We note that Ro_f is more sensitive to metallicity when it is expressed as a function of the stellar mass M_* rather than the effective temperature T_{eff} . We can understand this through A19's evolutionary tracks: when we fix T_{eff} and increase $[Fe/H]$ from -1 to $+0.3$, there is no significant change in structure or convective power (1% difference in r_{BCZ}/R_* and a difference of a factor of 2 in the mean convective velocity), hence no strong change in Ro_f . However, when we now fix M_* and apply the same increase in $[Fe/H]$, we note a significant decrease in convective power, leading to a drop in Ro_f by almost a factor of 10. Hence, the fluid Rossby number is more sensitive to metallicity effects when it is expressed with M_* .

Similarly to Sect. 2.3.4, it is convenient to consider a solar reference such that

$$\frac{Ro_f}{Ro_{f,\odot}} = \left(\frac{P_{\text{rot},*}}{P_{\text{rot},\odot}} \right) \times \left(\frac{T_{\text{eff}}}{T_{\text{eff},\odot}} \right)^{3.29} \times \left(\frac{[Fe/H] + 2}{2} \right)^{-0.31}. \quad (25)$$

We now applied the same Rossby criterion as in the previous section.

4.2. Most promising targets at different metallicities

Following the method we described in Sect. 3.2, we applied similar steps of data processing to the whole S19-21 subsample I. First, we obtained a maximum value $Ro_f/Ro_{f,\odot} = 0.608$ when applying Eq. 25 to PMS phases to the evolutionary tracks of A19. This again confirms that no explicit filtering of PMS stars is necessary. Then, the filtering we applied to exclude subgiants was adapted for each metallicity available in A19 (see details in Appendix A), which allowed us now to consider the range of metallicities $-1 < [Fe/H] < +0.3$ dex. After this data processing, we obtained 37,237 targets on which we applied Eq. 25. We clearly

Table 2. List and stellar parameters of anti-solar candidates beyond the solar metallicity range

KIC	$\log_{10}g$	T_{eff} [K]	P_{rot} [days]	$Ro_f/Ro_{f,\odot}$	[Fe/H]	M_* [M_{\odot}]	S_{ph} [ppm]	Zfl	Sfl
2161400	$4.44^{+0.04}_{-0.04}$	$6013.9^{+120.4}_{-117.3}$	48.7 ± 5.6	$2.19^{+0.29}_{-0.29}$	$-0.39^{+0.06}_{-0.06}$	$0.93^{+0.06}_{-0.06}$	253.3 ± 7.7	1	1
6842602	$4.56^{+0.01}_{-0.02}$	$6130.5^{+110.7}_{-105.0}$	40.9 ± 5.2	$2.07^{+0.30}_{-0.29}$	$-0.66^{+0.14}_{-0.15}$	$0.90^{+0.02}_{-0.03}$	409.3 ± 13.8	2	1
7097538	$4.40^{+0.04}_{-0.04}$	$5875.1^{+111.7}_{-109.2}$	47.7 ± 6.5	$1.91^{+0.29}_{-0.29}$	$-0.20^{+0.04}_{-0.04}$	$0.94^{+0.07}_{-0.07}$	370.8 ± 9.7	1	1
3628076	$4.43^{+0.04}_{-0.04}$	$5879.5^{+121.6}_{-120.5}$	43.3 ± 5.8	$1.82^{+0.27}_{-0.27}$	$-0.43^{+0.02}_{-0.02}$	$0.87^{+0.06}_{-0.06}$	545.7 ± 13.6	1	1
3113301	$4.11^{+0.03}_{-0.04}$	$5853.5^{+105.7}_{-101.2}$	47.7 ± 6.8	$1.76^{+0.27}_{-0.27}$	$0.29^{+0.03}_{-0.03}$	$1.26^{+0.05}_{-0.10}$	308.3 ± 7.1	1	1
10516429	$4.50^{+0.03}_{-0.04}$	$6036.6^{+131.6}_{-148.2}$	(36.6 ± 4.2)	$(1.75^{+0.24}_{-0.25})$	$-0.64^{+0.05}_{-0.05}$	$0.86^{+0.05}_{-0.06}$	204.2 ± 5.1	1	1
6356292	$4.47^{+0.04}_{-0.04}$	$5862.6^{+126.7}_{-119.8}$	38.4 ± 3.3	$1.68^{+0.19}_{-0.19}$	$-0.67^{+0.05}_{-0.05}$	$0.82^{+0.06}_{-0.05}$	354.3 ± 13.6	1	1
6436380	$4.22^{+0.03}_{-0.04}$	$5999.2^{+115.3}_{-116.0}$	(40.0 ± 2.6)	$(1.62^{+0.15}_{-0.15})$	$0.16^{+0.02}_{-0.02}$	$1.19^{+0.06}_{-0.08}$	348.1 ± 7.7	1	1

Notes. Similar to the Table 1 for promising targets beyond the solar metallicity range. The normalized fluid Rossby number value is computed from Eq. 25.

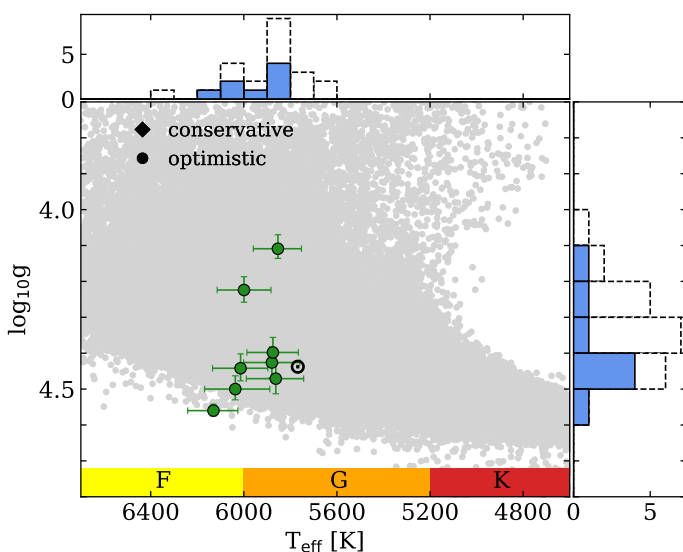


Fig. 3. Similar to Fig. 2 for anti-solar DR candidates beyond the solar metallicity range, summarized in Table 2. All of them are part of the optimistic sample. They are illustrated with green circles. Blue histograms on the x- and y-axes are proposed for the green dot sample. For comparison, we add dotted black histograms, which represent the whole set of candidates for all metallicities (i.e., the targets in Table 1 and 2).

found again all targets of Table 1 in the optimistic sample², and extended it by adding 37 new potential candidates. One of them was also in the conservative sample. Again we performed the individual visual inspections described in Sect. 3.3 and summarize the details in Appendix B. These inspections lead to eight new candidates, which are listed in Table 2 and illustrated in Fig. 3.

Table 2 shows that these eight new candidates are only in the optimistic sample. They show a rotation period between 36.6 and 48.7 days, T_{eff} from 5853 to 6131 K, M_* between 0.82 and 1.26 M_{\odot} , and [Fe/H] ranging from -0.67 to +0.29 dex. The S_{ph} values for all candidates fall within the solar values of 50 and 600 ppm at the minimum and maximum activity, respectively (Salabert et al. 2017). We note that KIC 3113301 and 6436380 show low $\log_{10}g$ while still being on the MS as they have a higher metallicity for a given T_{eff} . In contrast, the low-metallicity star

² Applying Eq. 25 on targets in Table 1 does not significantly change their $Ro_f/Ro_{f,\odot}$ values, as their [Fe/H] amplitude is small. The strongest change is experienced by KIC 10907436, which fluid Rossby increases from 2.44 to 2.47.

KIC 6842602 shows a significantly high $\log_{10}g$. Finally, we also considered a new P_{rot} for KIC 10516429 and 6436380 compared to the original catalog S19-21, resulting from a new period determination that was performed during the individual visual inspections. Original rotation periods in S19-21 are 47.7 ± 6.7 and 50.4 ± 9.0 days. Applying Eq. 25 to these targets with these new rotation periods, we still obtain Ro_f that is high enough to consider them in the optimistic sample.

Fig. 3 shows the eight candidates on a Kiel diagram. Blue histograms illustrate their distribution, located around the medians $\log_{10}g = 4.43$ and $T_{\text{eff}} = 5939$ K. We also show the distribution of the whole optimistic (for all metallicities) sample with dotted black histograms. This distribution is located around the medians $\log_{10}g = 4.37$ and $T_{\text{eff}} = 5869$ K, which is thus the parameter range in which Ro_f is highest and in which the anti-solar DR regime is likely to be reached for MS cool-stars for different metallicities.

Finally, we illustrate the whole set of the 22 considered optimistic targets in the left panel of Fig. 4 for all metallicities. This is a diagram of Ro_f as a function of T_{eff} and P_{rot} . The DR regimes presented in Fig. 1 are expected in different regions. Two gray transition regions represent the anti-solar or solar-type DR transition (close to $Ro_f = 1$), and the solar-type or cylindrical transition (close to $Ro_f=0.15$, Brun et al. 2017, 2022). The width of the transition is defined between the two solar values $Ro_{f,\odot}$ from Sect. 3.3. This translates into $Ro_f/Ro_{f,\odot} = (1.67, 1.11)$ and $(0.25, 0.16)$. We also show a zoom of this plot in the right panel and indicate the [Fe/H] value for each target on a color bar. We note that most of solar metallicity stars tend to cluster in the lower left corner. We find 4 targets in the transition region toward the anti-solar DR regime, and the other targets lie in the region in which an anti-solar DR regime is expected.

5. Discussion

We succeeded to obtain 22 stellar candidates that are likely to be in an anti-solar DR regime. We are confident about the robustness of the final sample thanks to different filtering methods and several individual visual inspections for each of the targets presented (see Sect. 3). However, some good candidates may have been missed during the different selection processes. They are discussed in this section.

To estimate Ro_f , we used P_{rot} values taken from the most recent and complete rotational catalog in date for the *Kepler* field (S19-21), where their P_{rot} measurements rely on rotational mod-

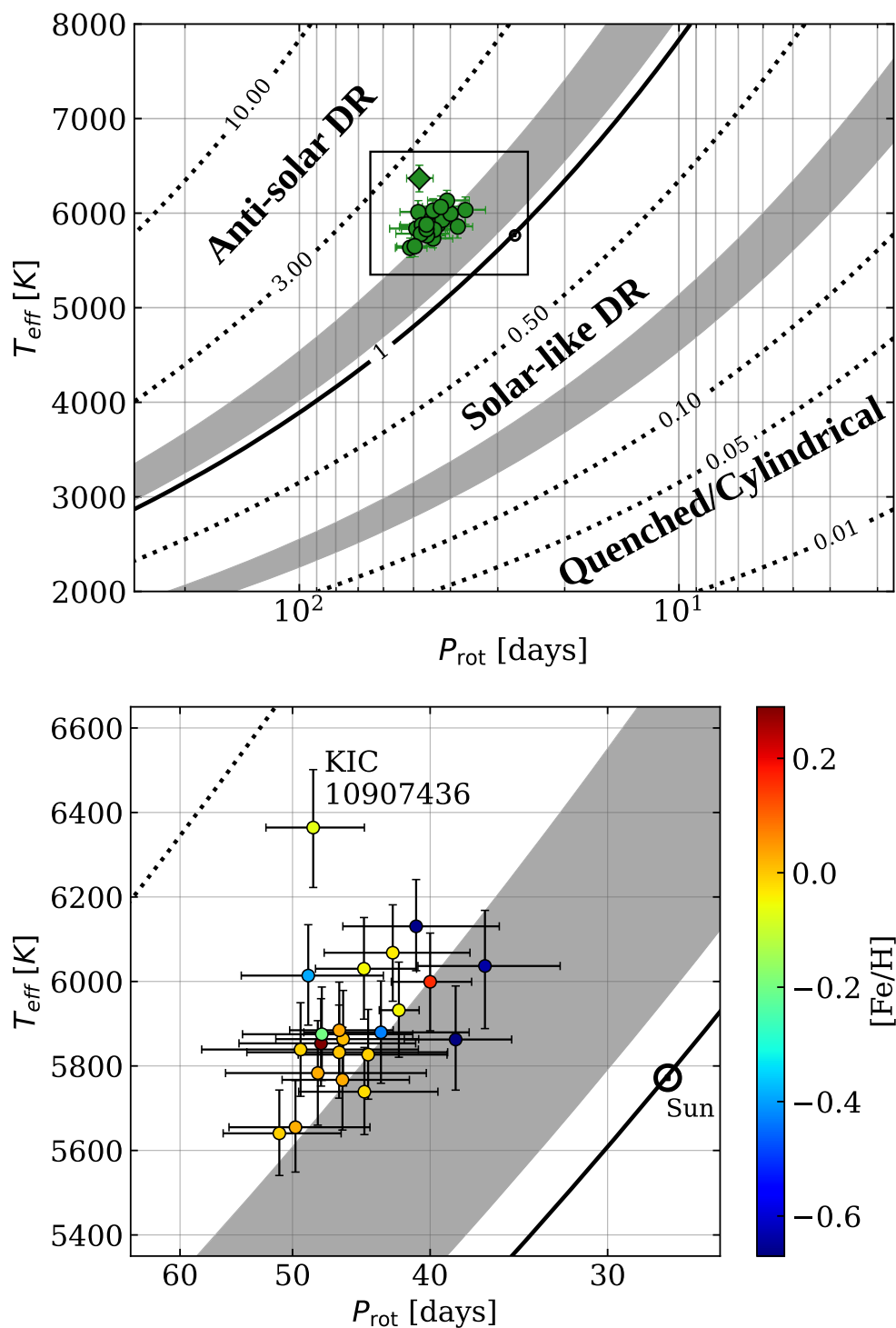


Fig. 4. DR diagram in which different DR regimes are expected: anti-solar, solar-type, and quenched or cylindrical (see Fig. 1). Gray regions represent transition regions between DR regimes. *Top*: Dotted lines represent constant $Ro_t/Ro_{t,\odot}$ as a function of T_{eff} and P_{rot} as deduced from Eq. 18. The solid black line represents the value $Ro_t/Ro_{t,\odot} = 1$. *Bottom*: Zoom into the top panel around the anti-solar DR candidates, color-coded by metallicity.

ulations from starspots in light curves. However, the exact nature of magnetic activity under anti-solar DR is still under debate from a numerical point of view (Karak et al. 2015; Viviani et al. 2019), first concerning the possibility of long-term cyclic solutions (Karak et al. 2020, Noraz et al. 2022 and references therein). Moreover, global numerical simulations currently do not self-consistently resolve starspots. Hence, even if most dynamo simulations highlight stationary configurations, we do not

have clues about the starspot formation rate and behavior in a high Rossby number regime. The detection of their modulation in photometric light curves is thus questionable and could be hard, which might explain the relatively small number of promising targets our method selected in the *Kepler* field.

Observations of Brandenburg & Giampapa (2018) have reported high Rossby targets that show an increase in chromospheric variability compared to the decreasing trend that is ex-

pected with the Rossby number. They argued that this enhanced activity for slow rotators could be caused by an anti-solar DR regime. Nevertheless, we would add here that it currently appears to be hard to distinguish whether these strong variabilities are due to an anti-solar DR regime or are caused by tidally triggered magnetic activity in multiple-stars system (e.g., Schrijver & Zwaan 1991; Kóvári et al. 2021). These targets are indeed statistically isolated in the parameter space for slow rotators (see the large S_{ph} in Fig. 14 of Santos et al. 2021), which could also be an indication for unusually high magnetic activity.

We note that the 22 high Rossby targets that were finally retained as promising candidates for anti-solar rotation in our study do not exhibit S_{ph} values that are significantly higher (< 752 ppm) than those observed on the Sun (see Salabert et al. 2017). We also note that 25 out of 99 targets have higher S_{ph} values (> 1000 ppm), but they were discarded each time during visual inspections because they were likely to be polluted by a neighbor or by instrumental effects (details are available in Appendix B).

Another explanation for the relatively small number of candidates we found would be a less efficient angular momentum loss for old solar-type stars. A stalled wind-braking mechanism at later stages may prevent stars from entering the high Rossby number regime. This has indeed been observed through photometry (van Saders et al. 2016) and asteroseismology techniques (Hall et al. 2021). However, this question is still debated in the community, and we refer to Sect. 1 of this paper for other details.

Moreover, the method we proposed to determine the transition between the MS and subgiant phase is a first approximation. Even if linear fits in the parameter space ($\log_{10}g$; T_{eff}) are good approximations for most of the models taken from A19 (see details in Appendix A), a more accurate characterization of the evolutionary stage of the stars in this transition region would require an asteroseismic analysis. For the same reason, MS cool stars near the end of the MS might have been filtered with our method because of relatively high $\log_{10}g$ or relatively low T_{eff} . Older stars are more likely to be slow rotators, which makes them good candidates for hosting a high Rossby number. Hence, we may have filtered out some promising anti-solar candidates.

Our selection method from the S19-21 rotation catalog did not select the anti-solar candidates proposed by Reinhold & Arlt (2015) or Benomar et al. (2018) as promising targets for hosting anti-solar DR. However, we note that because of the mode suppression by magnetic features, seismic targets tend to be only weakly active (e.g., Chaplin et al. 2011; Mathur et al. 2019). This also means that detecting the signature of surface rotation due to starspots for these targets might be difficult. Consequently, S19-21 were not able to determine photometric surface P_{rot} for all seismic targets in Benomar et al. (2018). Nevertheless, when we consider the rotation rates that were determined through asteroseismology by the authors, KIC 8938364 and 3427720 become interesting, and would fall in the anti-solar DR region and in the transition (gray area) of Fig. 4, respectively. Unfortunately, the associated error bars derived from this technique are large and prevent us from considering these targets as promising. We also searched for candidates among the LEGACY/Kepler seismic targets of Lund et al. (2017) and Hall et al. (2021) for which no photometric period was detected and failed to find any targets that clearly passed our selection process.

To be consistent with the mass estimates we considered from S19-21, we took the [Fe/H] values from B20, which come mostly from isochrone fittings, and thus give relatively large error bars. Nevertheless, for half of the final candidates, the [Fe/H] values come from spectroscopic observations, which are known to be

more precise in general. We also note that seven of the eight candidates outside the solar metallicity range, for which the Ro_f computation takes metallicity into account, have spectroscopic [Fe/H] values (see Table 2). Therefore, our selection method may have missed targets with inaccurate [Fe/H], but our final sample is likely quite robust in this respect.

6. Conclusion

In conclusion, we presented a novel approach for highlighting the most promising candidates for the detection of anti-solar DR regime in MS cool stars. We proposed a first application of our method to the *Kepler* field.

We first derived an analytical formula to quantify the fluid Rossby number Ro_f from observational quantities (P_{rot} , T_{eff}) while taking the structural aspect of solar-type stars into account. After calibrating it with evolutionary tracks of A19, we then applied this formula to the new S19-21 rotation catalog of the *Kepler* field. A first selection was made on stars in the solar metallicity range ($-0.1 \text{ dex} < [\text{Fe}/\text{H}] < +0.1 \text{ dex}$) with a criterion inspired from recent global MHD numerical simulations (B22). We took care to properly filter pre-MS and post-MS stars in our analysis and finally inspected each selected target to ensure the reliability of the Ro_f values we computed.

Next, we extended the derivation of Ro_f to add a dependence on the metallicity, which can notably change the structure of stars for a given mass. We adapted our filtering method and considered targets with a metallicity between $[\text{Fe}/\text{H}] = -1$ and $+0.3 \text{ dex}$.

This study finally gives us 22 anti-solar DR stellar candidates, 14 of which are at the solar metallicity. We especially note KIC 10907436, which has a significantly high Ro_f and is therefore one of the most promising candidates for the anti-solar DR regime. Four solar analogs (KIC 6068129, 6850029, 742872, and 7189915) are also particularly interesting due to their long P_{rot} (between 44.2 and 51.1 days) for the study of the future evolution of the Sun. More generally, all 22 targets possess P_{rot} between 36.6 and 51.1 days for spectral types between $T_{\text{eff}} = 5641$ and 6364 K. The determination of their age could therefore give new insights into the debate about the gyrochronology break for old solar-type stars, and more generally, for their rotational evolution (Curtis et al. 2020; David et al. 2022). Another noteworthy candidate is KIC 12117868, which is a seismic target. It could therefore be of interest for future measurements or characterizations, in particular, for its latitudinal rotation profile through asteroseismic inversions (Benomar et al. 2018), in order to confirm or refute that it has an anti-solar rotation profile.

Anti-solar DR detections on MS cool stars would provide useful observational constraints to better understand the link between rotation and magnetism of slowly rotating stars. Long-term observations would bring constraints on their magnetic activity and would therefore help to determine whether anti-solar differentially rotating stars could sustain magnetic cycles (Karak et al. 2020; Noraz et al. 2021). Such constraints for solar analogs would also help to decipher what types of dynamo mechanisms are acting within our Sun (Brun et al. 2022).

To conclude, this paper was a first attempt to compute Ro_f from observations and to apply this method to the *Kepler* field. The analytical development of the fluid Rossby number is generic and could be applied to the field of future missions such as PLAnetary Transits and Oscillations of stars (PLATO, Rauer et al. 2014).

Acknowledgements. QN is thankful to J. Ahuir, A. Finley, L. Gizon, S. Jeffers and T. Reinhold for useful discussions. We acknowledge financial sup-

port by ERC Whole Sun Synergy grant #810218., funding by INSU/PNST grant, CNES/Solar Orbiter, CNES/PLATO, and CNES/GOLF funds. ARGES acknowledges the supported by FCT through national funds and by FEDER through COMPETE2020 by these grants: UIDP/04434/2020; PTDC/FIS-AST/30389/2017 & POCI-01-0145-FEDER-030389. ARGES is supported by FCT through the work contract No. 2020.02480.CECCIND/CP1631/CT0001. SM acknowledges support by the Spanish Ministry of Science and Innovation with the Ramon y Cajal fellowship number RYC-2015-17697 and the grant number PID2019-107187GB-I00. This paper includes data collected by the *Kepler* mission and obtained from the MAST data archive at the Space Telescope Science Institute (STScI). Funding for the *Kepler* mission is provided by the NASA Science Mission Directorate. STScI is operated by the Association of Universities for Research in Astronomy, Inc., under NASA contract NAS 5-26555. This publication also makes use of data products from the Two Micron All Sky Survey, which is a joint project of the University of Massachusetts and the Infrared Processing and Analysis Center/California Institute of Technology, funded by the National Aeronautics and Space Administration and the National Science Foundation. We also thank the *Kepler* Asteroseismic Science Operations Center, KASOC, and the Aarhus University for maintaining this website. Finally, we thank the anonymous referee for constructive comments that have led to the improvement of the manuscript.

References

- Abdurro'uf, Accetta, K., Aerts, C., et al. 2022, arXiv:2112.02026 [astro-ph] [arXiv:2112.02026]
- Ahumada, R., Prieto, C. A., Almeida, A., & Anders, F. 2020, *The Astrophysical Journal Supplement Series*, 21
- Amard, L. & Matt, S. P. 2020, *The Astrophysical Journal*, 889, 108
- Amard, L., Palacios, A., Charbonnel, C., et al. 2019, *Astronomy & Astrophysics*, 631, A77
- Barnes, S. A. 2003, *The Astrophysical Journal*, 586, 464
- Benomar, O., Bazot, M., Nielsen, M. B., et al. 2018, *Science*, 361, 1231
- Berger, T. A., Huber, D., van Saders, J. L., et al. 2020, *The Astronomical Journal*, 159, 280
- Borucki, W. J., Koch, D., Basri, G., et al. 2010, *Science*, 327, 977
- Brandenburg, A. & Giampapa, M. S. 2018, *The Astrophysical Journal*, 855, L22
- Breton, S. N., Santos, A. R. G., Bugnet, L., et al. 2021, *A&A*, 647, A125
- Brun, A. S. 2004, *Solar Physics*, 220, 333
- Brun, A. S. & Browning, M. K. 2017, *Living Reviews in Solar Physics*, 14
- Brun, A. S., Strugarek, A., Noraz, Q., et al. 2022, *The Astrophysical Journal*, 926, 21
- Brun, A. S., Strugarek, A., Varela, J., et al. 2017, *The Astrophysical Journal*, 836, 192
- Cat, P. D., Fu, J. N., Ren, A. B., et al. 2015, *The Astrophysical Journal Supplement Series*, 220, 19
- Cayrel de Strobel, G. 1996, *Astronomy and Astrophysics Review*, 7, 243
- Ceillier, T., Tayar, J., Mathur, S., et al. 2017, *A&A*, 605, A111
- Ceillier, T., van Saders, J., García, R. A., et al. 2016, *MNRAS*, 456, 119
- Chaplin, W. J., Bedding, T. R., Bonanno, A., et al. 2011, *ApJL*, 732, L5
- Corsaro, E., Bonanno, A., Mathur, S., et al. 2021, *Astronomy & Astrophysics*, 652, L2
- Cranmer, S. R. & Saar, S. H. 2011, *The Astrophysical Journal*, 741, 54
- Curtis, J. L., Agüeros, M. A., Matt, S. P., et al. 2020, *The Astrophysical Journal*, 904, 140
- David, T. J., Angus, R., Curtis, J. L., et al. 2022, arXiv:2203.08920 [astro-ph] [arXiv:2203.08920]
- do Nascimento Jr., J.-D., de Almeida, L., Velloso, E. N., et al. 2020, *The Astrophysical Journal*, 898, 173
- Elliott, J. R., Miesch, M. S., & Toomre, J. 2000, *ApJ*, 533, 546
- Emeriau-Viard, C. & Brun, A. S. 2017, *The Astrophysical Journal*, 846, 8
- Fan, Y. & Fang, F. 2014, *The Astrophysical Journal*, 789, 35
- Finley, A. J. & Matt, S. P. 2018, *The Astrophysical Journal*, 854, 78
- Gallet, F. & Bouvier, J. 2013, *Astronomy & Astrophysics*, 556, A36
- García, R. A., Hekker, S., Stello, D., et al. 2011, *MNRAS*, 414, L6
- García, R. A., Mathur, S., Pires, S., et al. 2014, *A&A*, 568, A10
- García, R. A., Mathur, S., Salabert, D., et al. 2010, *Science*, 329, 1032
- García, R. A. & Ballot, J. 2019, *Living Reviews in Solar Physics*, 16, 4
- García, R. A., Ceillier, T., Salabert, D., et al. 2014, *Astronomy & Astrophysics*, 572, A34
- Gastine, T., Yadav, R. K., Morin, J., Reiners, A., & Wicht, J. 2014, *Monthly Notices of the Royal Astronomical Society: Letters*, 438, L76
- Gilman, P. A. 1975, *Journal of Atmospheric Sciences*, 32, 1331
- Gilman, P. A. 1977, *Geophysical and Astrophysical Fluid Dynamics*, 8, 93
- Guerrero, G., Smolarkiewicz, P. K., Kosovichev, A. G., & Mansour, N. N. 2013, *The Astrophysical Journal*, 779, 176
- Habets, G. M. H. J. & Heintze, J. R. W. 1981, *A&AS*, 46, 193
- Hall, O. J., Davies, G. R., van Saders, J., et al. 2021, *Nature Astronomy*, 5, 707
- Hanasoge, S., Miesch, M. S., Roth, M., et al. 2015, *Space Science Reviews*, 196, 79
- Harutyunyan, G., Strassmeier, K. G., Künstler, A., Carroll, T. A., & Weber, M. 2016, *Astronomy & Astrophysics*, 592, A117
- Jenkins, J. M., Caldwell, D. A., Chandrasekaran, H., et al. 2010, *ApJL*, 713, L87
- Käpylä, P. J., Mantere, M. J., & Brandenburg, A. 2011, *Astronomische Nachrichten*, 332, 883
- Karak, B. B., Käpylä, P. J., Käpylä, M. J., et al. 2015, *Astronomy & Astrophysics*, 576, A26
- Karak, B. B., Tomar, A., & Vashishth, V. 2020, *Monthly Notices of the Royal Astronomical Society*, 491, 3155
- Karoff, C., Metcalfe, T. S., Santos, A. R. G., et al. 2018, *The Astrophysical Journal*, 852, 46
- Kippenhahn, R., Weigert, A., & Weiss, A. 2012, *Stellar Structure and Evolution*, *Astronomy and Astrophysics Library* (Berlin, Heidelberg: Springer Berlin Heidelberg)
- Kjeldsen, H., Christensen-Dalsgaard, J., Handberg, R., et al. 2010, *Astronomische Nachrichten*, 331, 966
- Käpylä, P. J., Käpylä, M. J., & Brandenburg, A. 2014, *Astronomy & Astrophysics*, 570, A43
- Kovári, Z., Kriskovics, L., Oláh, K., et al. 2021, *Astronomy & Astrophysics*, 650, A158
- Kovári, Z., Strassmeier, K. G., Carroll, T. A., et al. 2017, *Astronomy & Astrophysics*, 606, A42
- Landin, N. R., Mendes, L. T. S., & Vaz, L. P. R. 2010, *Astronomy and Astrophysics*, 510, A46
- Lebreton, Y. & Goupil, M. J. 2014, *Astronomy & Astrophysics*, 569, A21
- Lorenzo-Oliveira, D., Meléndez, J., Yana Galarza, J., et al. 2019, *Monthly Notices of the Royal Astronomical Society: Letters*, 485, L68
- Lund, M. N., Aguirre, V. S., Davies, G. R., et al. 2017, *The Astrophysical Journal*, 835, 172
- Mabuchi, J., Masada, Y., & Kageyama, A. 2015, *The Astrophysical Journal*, 806, 10
- Maeder, A. 2009, *Physics, Formation and Evolution of Rotating Stars*, ed. G. Börner, A. Burkert, W. B. Burton, M. A. Dopita, A. Eckart, T. Encenaz, E. K. Grebel, B. Leibundgut, A. Maeder, & V. Trimble, *Astronomy and Astrophysics Library* (Berlin, Heidelberg: Springer Berlin Heidelberg)
- Mathur, S., García, R. A., Ballot, J., et al. 2014, *A&A*, 562, A124
- Mathur, S., García, R. A., Breton, S., et al. 2022, *Astronomy & Astrophysics*, 657, A31
- Mathur, S., García, R. A., Bugnet, L., et al. 2019, *Frontiers in Astronomy and Space Sciences*, 6, 46
- Mathur, S., Huber, D., Batalha, N. M., et al. 2017, *The Astrophysical Journal Supplement Series*, 229, 30
- Mathur, S., Salabert, D., García, R. A., & Ceillier, T. 2014, *Journal of Space Weather and Space Climate*, 4, A15
- Matt, S., Do Cao, O., Brown, B., & Brun, A. 2011, *Astronomische Nachrichten*, 332, 897
- McQuillan, A., Mazeh, T., & Aigrain, S. 2014, *ApJS*, 211, 24
- Mestel, L. 1968, *Monthly Notices of the Royal Astronomical Society*, 138, 359
- Metcalfe, T. S., Kochukhov, O., Ilyin, I. V., et al. 2019, *The Astrophysical Journal*, 887, L38
- Miesch, M. S., Brun, A. S., & Toomre, J. 2006, *The Astrophysical Journal*, 641, 618
- Noraz, Q., Brun, A. S., Strugarek, A., & Depambour, G. 2022, *Astronomy & Astrophysics*, 658, A144
- Noraz, Q., Brun, S., & Strugarek, A. 2021, in *SF2A-2021: Proceedings of the Annual meeting of the French Society of Astronomy and Astrophysics*. Eds.: A. Siebert, ed. A. Siebert, K. Baillie, E. Lagarde, N. Lagarde, J. Malzac, J. B. Marquette, M. N'Diaye, J. Richard, & O. Venot, 226–229
- Noyes, R. W., Weiss, N. O., & Vaughan, A. H. 1984, *The Astrophysical Journal*, 287, 769
- Pires, S., Mathur, S., García, R. A., et al. 2015, *A&A*, 574, A18
- Prša, A., Harmanec, P., Torres, G., et al. 2016, *The Astronomical Journal*, 152, 41
- Rauer, H., Catala, C., Aerts, C., et al. 2014, *Experimental Astronomy*, 38, 249
- Reinhold, T. & Arlt, R. 2015, *Astronomy & Astrophysics*, 576, A15
- Reinhold, T. & Gizon, L. 2015, *Astronomy & Astrophysics*, 583, A65
- Réville, V., Brun, A. S., Matt, S. P., Strugarek, A., & Pinto, R. F. 2015, *The Astrophysical Journal*, 798, 116
- Salabert, D., García, R. A., Jiménez, A., et al. 2017, *Astronomy & Astrophysics*, 608, A87
- Santos, A. R. G., Breton, S. N., Mathur, S., & García, R. A. 2021, *The Astrophysical Journal Supplement Series*, 255, 17
- Santos, A. R. G., Cunha, M. S., Avelino, P. P., García, R. A., & Mathur, S. 2017, *Astronomy & Astrophysics*, 599, A1
- Santos, A. R. G., García, R. A., Mathur, S., et al. 2019, *ApJS*, 244, 21
- Schatzman, E. 1962, *Annales d'Astrophysique*, 25, 18

- Schrijver, C. J. & Zwaan, C. 1991, A&A, 251, 183
- See, V., Matt, S. P., Finley, A. J., et al. 2019, The Astrophysical Journal, 886, 120
- See, V., Roquette, J., Amard, L., & Matt, S. P. 2021, The Astrophysical Journal, 912, 127
- Simitev, R. D., Kosovichev, A. G., & Busse, F. H. 2015, The Astrophysical Journal, 810, 80
- Skrutskie, M. F., Cutri, R. M., Stiening, R., et al. 2006, The Astronomical Journal, 131, 1163
- Skumanich, A. 1972, ApJ, 171, 565
- Smith, J. C., Stumpe, M. C., Van Cleve, J. E., et al. 2012, PASP, 124, 1000
- Strassmeier, K. G., Kratzwald, L., & Weber, M. 2003, Astronomy & Astrophysics, 408, 1103
- Strugarek, A., Beaudoin, P., Charbonneau, P., & Brun, A. S. 2018, The Astrophysical Journal, 863, 35
- Stumpe, M. C., Smith, J. C., Van Cleve, J. E., et al. 2012, PASP, 124, 985
- Van Cleve, J. E. & Caldwell, D. A. 2016, Kepler Instrument Handbook, Kepler Science Document KSCI-19033-002, id.1. Edited by Michael R. Haas and Steve B. Howell
- van Saders, J. L., Ceillier, T., Metcalfe, T. S., et al. 2016, Nature, 529, 181
- Vidotto, A. A. 2021, 86
- Viviani, M., Käpylä, M. J., Warnecke, J., Käpylä, P. J., & Rheinhardt, M. 2019, The Astrophysical Journal, 886, 21
- Warnecke, J. 2018, Astronomy & Astrophysics, 616, A72
- Weber, E. J. & Davis, Leverett, J. 1967, ApJ, 148, 217
- Zhao, G., Zhao, Y.-H., Chu, Y.-Q., Jing, Y.-P., & Deng, L.-C. 2012, Research in Astronomy and Astrophysics, 12, 723
- Zong, W., Fu, J.-N., Cat, P. D., et al. 2018, The Astrophysical Journal Supplement Series, 238, 30
- Ó Fionnagáin, D. & Vidotto, A. A. 2018, Monthly Notices of the Royal Astronomical Society, 476, 2465

Appendix A: TAMS as a function of the metallicity

It is a difficult task to observationally distinguish between evolved MS stars and young subgiants. In this situation, an arbitrary choice has to be made in order to filter out stars from the MS populations that might be subgiants. Because we wished to select only cool MS stars in this study, we chose an approach similar to what was considered by S19-21. We thus fit stellar evolution models of A19 at the TAMS as a function of $\log_{10}g$ and T_{eff} for a given $P_{\text{rot,ini}}$ and a given $[\text{Fe}/\text{H}]$. This gives us a limit in a Kiel diagram (e.g., Fig. 2) above which the stars are considered subgiants. We did this for 7 $[\text{Fe}/\text{H}]$ values between +0.3 and -1.0 for slow and medium rotators. We did not consider the fast rotators because their rotational history was specifically treated for the most massive stars (see Sect. 2.6.1 of A19). Moreover, we expect anti-solar DR profiles to appear for slowly rotating stars. Slopes δ and y-intercepts ξ of the TAMS($\log_{10}g$, T_{eff}) regressions are reported in Table A.1.

We then determined the behavior of δ and ξ as functions of the metallicity index $[\text{Fe}/\text{H}]$ through linear regressions (see Fig. A.1), which gives

$$\delta([\text{Fe}/\text{H}]) = ((-34.36 \pm 1.81) \times [\text{Fe}/\text{H}] + (-39.63 \pm 0.83)) \cdot 10^{-5} \quad (\text{A.1})$$

$$\xi([\text{Fe}/\text{H}]) = (1.84 \pm 0.14) \times [\text{Fe}/\text{H}] + 6.49 \pm 0.06 - 0.12 \cdot \quad (\text{A.2})$$

We note that the resulting ξ has to be shifted toward low $\log_{10}g$ values (-0.12 dex) in order to be compatible with $\log_{10}g$ of S19-21. These two equations are valid for $+0.3 \geq [\text{Fe}/\text{H}] \geq -1.0$, that is, the range of metallicities in the A19 evolutionary grid. Finally, we confirm that subgiants do not exist for $T_{\text{eff}} < 5000\text{K}$ and $\log_{10}g < 4.4$ based on the tracks in this grid of A19. The Universe is currently too young to consider that MS stars in this temperature range have already left the MS. We finally illustrate some subgiant cuts in Fig. A.2.

Table A.1. Parameters of the different linear regression at the TAMS in order to determine subgiant cuts in a Kiel diagram.

$P_{\text{rot,ini}}$ (days)	$[\text{Fe}/\text{H}]$	δ	ξ
9	-1.00	$(-3.64 \pm 1.01) \times 10^{-5}$	4.46 ± 0.08
9	-0.50	$(-1.87 \pm 0.29) \times 10^{-4}$	5.35 ± 0.19
9	-0.30	$(-2.95 \pm 0.47) \times 10^{-4}$	6.00 ± 0.31
9	-0.15	$(-3.36 \pm 0.65) \times 10^{-4}$	6.22 ± 0.42
9	0.00	$(-3.71 \pm 0.39) \times 10^{-4}$	6.36 ± 0.23
9	0.15	$(-4.69 \pm 0.40) \times 10^{-4}$	6.86 ± 0.23
9	0.30	$(-4.84 \pm 0.43) \times 10^{-4}$	6.88 ± 0.24
4.5	-1.00	$(-6.10 \pm 2.33) \times 10^{-5}$	4.67 ± 0.17
4.5	-0.50	$(-2.41 \pm 0.33) \times 10^{-4}$	5.70 ± 0.22
4.5	-0.30	$(-3.39 \pm 0.65) \times 10^{-4}$	6.28 ± 0.42
4.5	-0.15	$(-3.70 \pm 0.69) \times 10^{-4}$	6.43 ± 0.44
4.5	0.00	$(-3.73 \pm 0.41) \times 10^{-4}$	6.37 ± 0.24
4.5	0.15	$(-4.66 \pm 0.40) \times 10^{-4}$	6.85 ± 0.23
4.5	0.30	$(-4.90 \pm 0.45) \times 10^{-4}$	6.91 ± 0.25

Notes. We regrouped the slopes δ and y-intercepts ξ of the different linear regressions, with the corresponding $P_{\text{rot,ini}}$ in days and metallicity index $[\text{Fe}/\text{H}]$.

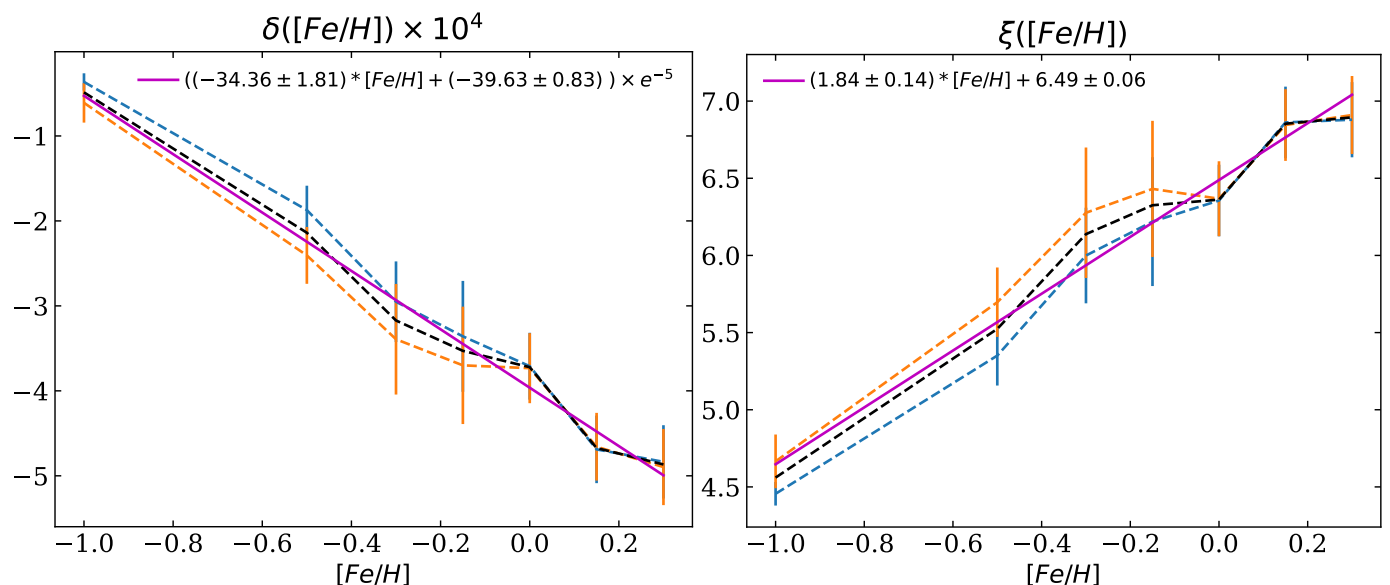


Fig. A.1. *Left:* δ slopes from Table A.1 as a function of $[Fe/H]$. Orange and blue correspond to medium and slow rotators, respectively. The dotted black line represents the δ mean for each metallicity index of the table, and the purple line is a linear regression of these mean values. *Right:* Similar to the left panel for y-intercepts ξ .

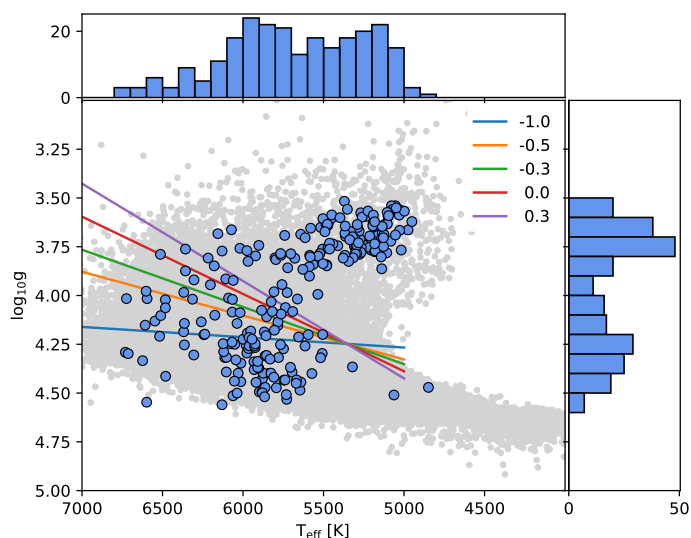


Fig. A.2. Kiel diagram of the optimistic sample by applying Eq. 25 to the whole S19-21 rotation catalog before filtering masses, metallicities, and subgiants and before individual inspections. Histograms are illustrated in blue on both axes for the selected targets. We show subgiant cuts for different metallicities computed with Eq. A.2 in the same diagram.

Appendix B: Detailed method of individual light-curve inspections and additional rotation diagnostics

We detail here the different verifications we performed in the step 4 of individual inspections as discussed in Sect. 3.2. For each target in the optimistic sample, we inspected the three KEPSEISMIC light curves used in S19-21 and the Presearch Data Conditioning - Maximum A Posteriori (PDC-MAP; e.g., Jenkins et al. 2010; Smith et al. 2012; Stumpe et al. 2012) light curve. KEPSEISMIC light curves were obtained with *Kepler* Asteroseismic Data Analysis and Calibration Software (KADACS; García et al. 2011), which employs customized apertures and

corrects for outliers, jumps, drifts, and discontinuities at the edges of the *Kepler* quarters. Gaps smaller than 20 days were filled using inpainting techniques (García et al. 2014; Pires et al. 2015). Finally, we applied three filters with cutoff periods at 20, 55, and 80 days, resulting in three KEPSEISMIC light curves per star. It was crucial to filter the data to remove instrumental modulations, but it can also filter the stellar signal. Thus, the three filtered light curves were analyzed in parallel. In spite of the data treatment, modulations related to the *Kepler* year and quarters are still present in the light curves of some targets. For this reason and because we are interested in relatively slow rotators whose signal is most affected by instrumental artifacts, we obtained three additional KEPSEISMIC light curves. For these, the long-term *Kepler* modulation was subtracted from the light curve before the filters were applied. To do this, the autocorrelation function (ACF) of the light curve was computed and the maximum around ± 30 days of the *Kepler* orbital period (372.5 days) was determined, hereafter P_{Kepler} . The original data were then phase-folded with P_{Kepler} , and the resulting curve was fit with a third-degree polynomial. To detrend the light curve, each segment of the length P_{Kepler} was corrected by subtracting the fitted curve linearly scaled from the data in this segment. This procedure minimized any trends around the *Kepler* orbital period in the light curve for most of the targets. Nevertheless, when the retrieved P_{rot} with the new calibration was compatible with the period given in S19-21, we kept the latter for the sake of clarity. The parallel inspection of the seven light curves and respective rotation diagnostics allowed us to verify the nature of the signal. The rotation diagnostics were a wavelet analysis, an autocorrelation function, and their composite spectrum. We also visually inspected the power spectrum density of each light curve. For details about the rotation diagnostics, see S19-21 and references therein.

The results of these individual visual inspections are listed in Table B.1 for all targets of the optimistic sample. The full version of the table along with the data of all 99 solar-type stars of this sample are available online (62 stars at solar metallicity and 37

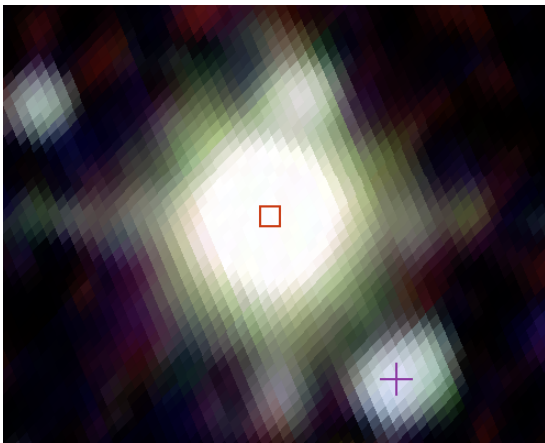


Fig. B.1. Image from the KASOC website of KIC 10934680 using Two Micron All Sky Survey (2MASS) images (Skrutskie et al. 2006). This star is marked by a purple cross, and it is in the halo of another *Kepler* target, KIC 10989776 (marked with a red square), whose *Kepler* magnitude is 2.5 times brighter.

stars with other metallicities)³. We discuss the examples listed in the short version of Table B.1 below.

The star KIC 10934680 is in the halo of KIC 10989776, a 2.5 times brighter star (halo flag 1; see Fig. B.1). We were unable to define the pollution clearly or clearly reject it, therefore the neighboring flag is noted 2. We therefore rejected this target from the final list of anti-solar candidates (candidate flag 0). The rotational modulation of the target is not clear either, which potentially biases the measured P_{rot} . We therefore set the P_{rot} flag to 1. Moreover, if no pollution from the neighboring star is found, we suspect that KIC 10934680 is a close multiple star system because the visible shape of this star is elongated (shape flag 1).

KIC 4042415 is also in the halo of a brighter star (halo flag 1), but this brighter star is distant and not visible in the *Kepler* acquisition FoV. However, the bright star clearly pollutes the light curve of target KIC 4042415 (P_{rot} flag as 1), so that we rejected this target. Moreover, a different close neighbor is visible in this FoV. It is far enough and not in the photometry aperture. Thus, the neighboring flag is 1, meaning that there is a close neighbor that does not pollute the light curve.

Individual inspections of KIC 5024984 do not show any sign of pollution by the halo of a brighter star (hence the halo flag is 0). We note that a neighbor (KIC 5024961) is visible in the 40'' \times 40'' FoV around our target, but does not pollute the signal we used (the neighboring flag is 1). Nevertheless, the related uncertainties of KIC 5024984 $\log_{10}g = 4.47^{+0.08}_{-0.75}$ are too high to decipher whether it is a subgiant or an MS star. We note that the value reported for this target in the DR25 catalog (Mathur et al. 2017) is significantly different and also highly uncertain: $\log_{10}g = 3.71^{+0.80}_{-0.27}$. As we performed a strict selection, we did not consider this target in our final sample of promising candidates (hence the $\log_{10}g$ flag is 1).

For KIC 3860063, we find a very close neighbor in the acquisition FoV that clearly pollutes the light curve. We therefore note the neighboring flag as 3. We further suspect that the large S_{ph} could result from a triggered activity by tidal interactions, which could indicate that both stars interact gravitationally (see the discussion in Sect. 5).

³ *Kepler* light curves and the rotation analysis we used to perform the individual visual inspections can be accessed along with a machine-readable form of Table B.1 through the following repository: <https://github.com/qnoraz/AntisolarCandidatesInspections.git>

The example KIC 6541604 shows no evidence for pollution from another star in the light curve. The new KEPSEISMIC light curves and their rotational analysis show that the P_{rot} extracted by S19-21 can be improved with the new treatment of the light curves. Hence, we are able to compute a better $P_{\text{rot}} = 66.0 \pm 11.5$ days, and then updated the Rossby number accordingly. We find $Ro_f/Ro_{f,\odot} = 1.57 \pm 0.29$. Its lower limit 1.28 is below the selection threshold $Ro_f/Ro_{f,\odot} = 1.3/0.9 = 1.44$. Thus, the P_{rot} flag is 2, and we did not consider this target in the final list of candidates.

The same conclusions hold for KIC 6436380, with a new rotation value of $P_{\text{rot}} = 40.0 \pm 2.56$ days. However, when the Rossby number was accordingly updated, we find $Ro_f/Ro_{f,\odot} = 1.62 \pm 0.15$, which is still above the selection threshold on Ro_f . Thus, we set the P_{rot} flag at 3 and consider KIC 6436380 as a candidate (see Table 2).

In the final example, we did not attest any pollution or close neighboring star for KIC 3113301. This target has a circular shape in the FoV, and the amplitude of its light-curve modulation is typical of stars with similar properties. Finally, the new KEPSEISMIC light curves and their rotational analysis (see Fig. B.2) confirm the reliability of its P_{rot} as extracted by S19-21. Hence, we set all the flags to 0 except for the last flag, which indicates that we consider this target as a candidate for anti-solar DR.

⁴ The full table is available in a machine-readable format at the public repository <https://github.com/qnoraz/AntisolarCandidatesInspections.git> and at the CDS via anonymous ftp to cdsarc.u-strasbg.fr (130.79.128.5) or via <http://cdsweb.u-strasbg.fr/cgi-bin/qcat?J/A+A/>.

Table B.1. Results of individual visual inspections.⁴

KIC	Halo flag [0,1]	Neighboring flag [0,1,2,3]	Shape flag [0,1]	$\log_{10}g$ flag [0,1]	P_{rot} flag [0,1,2,3]	Candidate flag [0,1]
...
3113301	0	0	0	0	0	1
...
3860063	0	3	0	0	1	0
...
4042415	1	1	0	0	1	0
...
5024984	0	1	0	1	0	0
...
6436380	0	1	0	0	3	1
...
6541604	0	1	0	0	2	0
...
10934680	1	2	1	0	1	0
...

Notes. Summary of the verifications made of the whole optimistic sample to determine whether a target is a reliable anti-solar DR candidate. The halo flag indicates whether the target is in the light halo of a brighter star from the visual inspection of 2MASS images (1) or not (0). The neighboring flag indicates whether a neighbor is at least visible in the *Kepler* acquisition FoV (1, 2, and 3) or not (0). If this is the case, we determined whether the main target light curve might be (2) or is clearly (3) polluting the target star, or if we acknowledge no pollution of the rotational signal (1). The shape flag indicates whether the shape of the target in the FoV is deformed or elongated, suggesting multiple stars (1) (possibly a close companion in the FOV), or not (0). The $\log_{10}g$ flag indicates whether an uncertainty in the $\log_{10}g$ value is suspiciously large and might cause us to consider a subgiant target. When we concluded during the inspection that the P_{rot} value extracted by S19-21 clearly derived from the rotational signal of the target (0) or not (1). If the light curve showed a rotational signal and we were able to improve the measurement and provide a new reliable P_{rot} , we provide flags 2 and 3. In this case, we indicate whether the new corresponding $Ro_f/Ro_{f,\odot}$ value is high enough to keep the target above the selection threshold and in the optimistic sample (3) (i.e., if the new lower limit of this value is higher than $1.3/0.9=1.44$) or not (2). We finally indicate with the candidate flag whether we consider the target as an anti-solar DR candidate (1) or not (0).

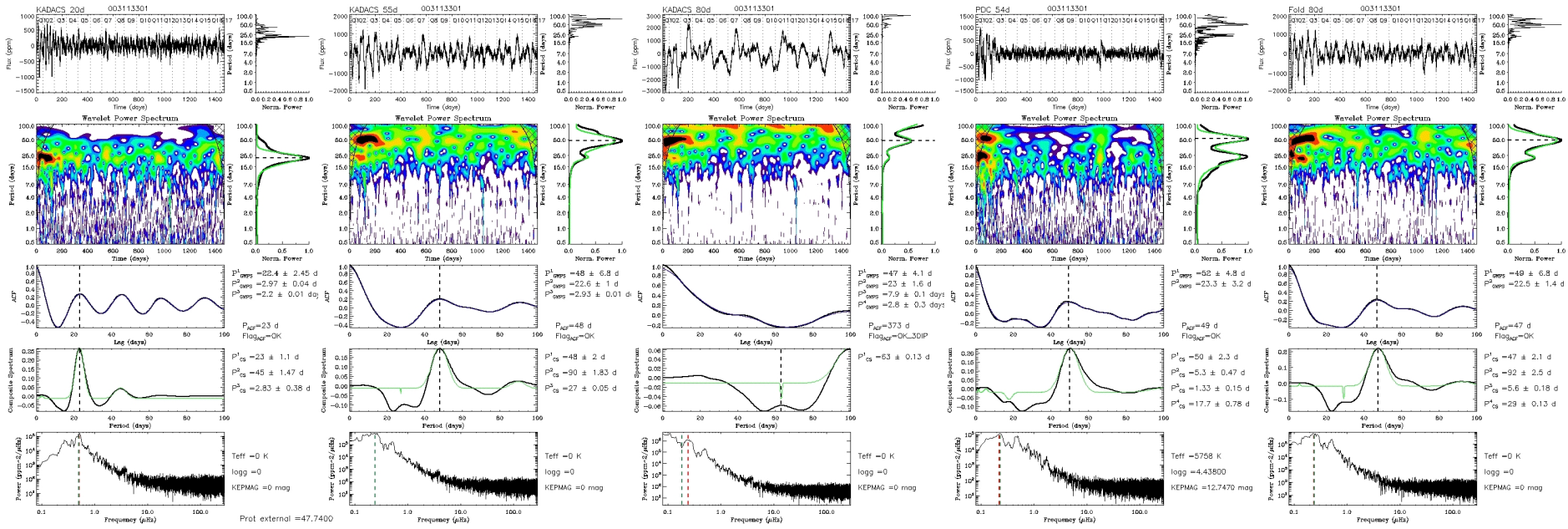


Fig. B.2. Example of one of the control plots for KIC 3113301. It contains the output of our rotation pipeline (see S19-21) for the three KEPEISMIC light curves in S19-21 (filtered at 20, 55, and 80d) for the PDC-MAP light curve (which in this example clearly filters the stellar rotation signature), and for the new KEPEISMIC light curve filtered at 80 days in which the modulation related to P_{Kepler} is removed. For a full description of the plots, we refer to S19-21. Briefly, from top to bottom we show the light curve and the Lomb-Scargle periodogram, the time-period analysis with the global wavelet power spectrum (GWPS), the ACF, the CS, and the full power spectrum density (PSD) in log-log scale.

Appendix C: Scaling laws

In order to determine the different exponents for equations 17 and 24, we performed linear regression fits, using a least-squares method in log space on stellar evolution models from A19. They proposed a grid of evolutionary tracks from the PMS to the TAMS for different initial rotation periods. Stellar masses ranged between 0.2 and $1.5M_{\odot}$, and metallicities were set for 7 [Fe/H] values from -1 to $+0.3$. We extracted the mean value of L_* , R_* , and $S(\alpha, \beta)$ during the MS for each model and performed regression fits as a function of M_* and [Fe/H], which we illustrate in Figure C.1.

As shown in the upper panels of Fig. C.1, multiparametric regressions give $m = m_1 = 4.66 \pm 0.03$ and $m_2 = -1.00 \pm 0.04$. We note that the regression was improved when we added the dependence on the metallicity (purple lines). This is shown in the top right corner, where we represent the reference values as a function of fitted values. The spread of dots around the dashed function $x = y$ is smaller for the blue (multiparametric relation) than for the orange dots (only with the M_* dependence). It is also visible in the uncertainties of the fit in the top left corner, which is smaller (± 0.03) when we prescribe a dependence on [Fe/H]. Similarly, we find $n = n_1 = 1.16 \pm 0.01$ in the second row, and we note that the quality of the regression is not improved significantly with a dependence on [Fe/H]. We find that R_* is not sensitive to the metallicity, with $n_2 = 0.01 \pm 0.01$. Finally, the third row shows that $q = q_1 = 1.48 \pm 0.05$ and $q_2 = -0.81 \pm 0.08$. We note that a power law is a good approximation for the homology relations in Eqs. 3 and 19, but it is a rough approximation for the structural term $S \propto M_*^q$ when we consider a range of masses that are too high. We therefore restricted our fits for $0.4 \leq M_* \leq 1.3M_{\odot}$, which defines the validity range for these regressions. Moreover, we note that the multiparametric regression of $S(\alpha, \beta)$ is much better than its single-parametric regression, which is shown with the dots that are spread in the lower right corner.

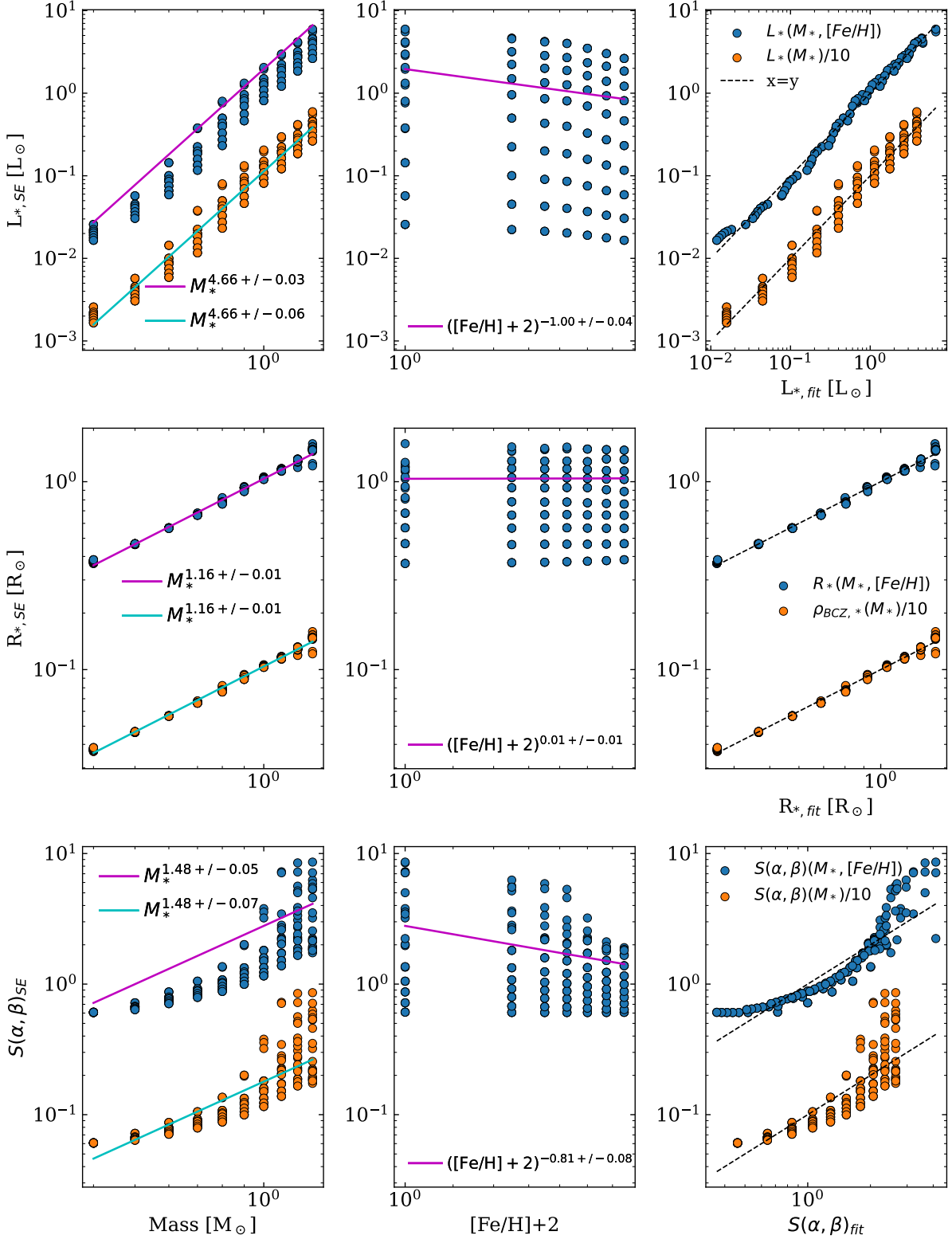


Fig. C.1. Linear regressions for determining the homology relations of Eqs. 3 and 19 and the structure term $S(\alpha, \beta)$ as defined in Eq. 13 and 20. We use the grid evolutionary track of A19 taken from the STAREVOL (SE) code. Each dot represents one of these stellar tracks, from which different values have been deduced as mean value during their MS (subscript SE). The first row shows L_* , the second row shows R_* , and the third row shows $S(\alpha, \beta)$. The first column illustrates these different values as a function of M_* , and the second column shows them as a function of $([Fe/H] + 2)$. The third column illustrates the quality of the fits. It represents the different original values (L_* , R_* , and $S(\alpha, \beta)$) as functions of the values that were estimated by the fits (subscript fit). These regressions are illustrated in the first and second columns. They are shown in purple if they are multiparametric (as a function of M_* and $[Fe/H]$) and in cyan when they are only a regression on M_* . Blue dots represent models on which we perform the multiparametric regression, and the orange group represents models on which we only fit on M_* . For the latter, we divided the values by 10 for illustration purposes.